JOURNAL OF PETROLOGY | VOLUME 48 | NUMBER 7 | PAGES 1265–1294 | 2007 | doi:10.1093/petrology/egm017

Role of Syn-eruptive Cooling and Degassing on Textures of Lavas from the AD 1783–1784 Laki Eruption, South Iceland

M.-N. GUILBAUD[1]*, S. BLAKE[1], T. THORDARSON[2] AND S. SELF[1]

[1]VOLCANO DYNAMICS GROUP, DEPARTMENT OF EARTH SCIENCES, THE OPEN UNIVERSITY, MILTON KEYNES MK7 6AA, UK

[2]SCHOOL OF GEOSCIENCES, UNIVERSITY OF EDINBURGH, GRANT INSTITUTE, WEST MAINS ROAD, EDINBURGH EH9 3JW, UK

RECEIVED AUGUST 3, 2006; ACCEPTED MARCH 10, 2007
ADVANCE ACCESS PUBLICATION APRIL 25, 2007

The Laki eruption involved 10 fissure-opening episodes that produced 15·1 km^3 of homogeneous quartz-tholeiite magma. This study focuses on the texture and chemistry of samples from the first five episodes, the most productive period of the eruption. The samples comprise pumiceous tephra clasts from early fallout deposits and lava surface samples from fire-fountaining and cone-building activity. The fluid lava core was periodically exposed at the surface upon lobe breakout, and its characteristics are preserved in glassy selvages from the lava surface. In all samples, plagioclase is the dominant mineral phase, followed by clinopyroxene and then olivine. Samples contain <7 vol. % of euhedral phenocrysts (>100 μm) with primitive cores [$An^* = 100 \times Ca/(Ca + Na)$ >70; $Fo > 75$; $En^* = 100 \times Mg/(Mg + Fe)$ >78] and more evolved rims, and >10 vol. % of skeletal, densely distributed groundmass crystals (<100 μm), which are similar in composition to phenocryst rims (tephra: $An^*_{58–67}$, $Fo_{72–78}$, $En^*_{72–81}$; lava: $An^*_{49–70}$, $Fo_{63–78}$, $En_{57–78}$). Tephra and lava have distinct vesicularity (tephra: >40 vol. %; lava: <40 vol. %), groundmass crystal content (tephra: <10 vol. %; lava: 20–30 vol. %), and matrix glass composition (tephra: 5·4–5·6 wt % MgO; lava: 4·3–5·0 wt % MgO). Whole-rock and matrix glass compositions define a trend consistent with liquid evolution during in situ *crystallization of groundmass phases. Plagioclase–glass and olivine–glass thermometers place the formation of phenocryst cores at ~10 km depth in a melt with ~1 wt % H_2O, at near-liquidus temperatures (~1150°C). Phenocryst rims and groundmass crystals formed close to the surface, at 10–40°C melt undercooling and in an ~10–20°C cooler drier magma (0–0·1 wt % H_2O), causing an ~10 mol % drop in An content in plagioclase. The shape, internal zoning and number density of groundmass crystals indicate that they formed under supersaturated conditions. Based on this information, we propose that degassing during ascent had a major role in rapidly undercooling the melt, prompting intensive shallow groundmass crystallization that affected the magma and lava rheology. Petrological and textural differences between tephra and lava reflect variations in the rates of magma ascent and the timing of surface quenching during each eruptive episode. That in turn affected the time available for crystallization and subsequent re-equilibration of the melt to surface (degassed) conditions. During the explosive phases, the rates of magma ascent were high enough to inhibit crystallization, yielding crystal-poor tephra. In contrast, pervasive groundmass crystallization occurred in the lava, increasing its yield strength and causing a thick rubbly layer to form during flow emplacement. Lava selvages collected across the flow-field have strikingly homogeneous glass compositions, demonstrating the high thermal efficiency of fluid lava transport. Cooling is estimated as 0·3°C/km, showing that rubbly surfaced flows can be as thermally efficient as tube-fed pāhoehoe lavas.*

KEY WORDS: *lava; crystallization; basalt; cooling rate; pressure; geobarometry;* P–T *conditions; plagioclase; degassing; Laki, Iceland*

INTRODUCTION

The presence of large numbers of small crystals (groundmass crystals) in a magma has a strong effect on its rheology. A yield strength develops at low crystal concentrations (above 20 vol. %) and is promoted by the formation of a crystalline framework (e.g. Pinkerton & Stevenson, 1992; Hoover *et al.*, 2001;

*Corresponding author. Present address: Instituto de Geofisica, Universidad Nacional Autonoma de México, Cuidad Universitaria, 04510 México D.F., Mexico. Telephone: (525) 622 4119 ext 22. Fax: (525) 550 2486. E-mail: m.guilbaud@geofisica.unam.mx

Saar *et al.*, 2001). Groundmass crystallization can thus trigger changes in eruptive style and eruption rate (e.g. Métrich *et al.*, 2001; Melnik & Sparks, 2002; Couch *et al.*, 2003; Polacci *et al.*, 2006) and may cause transitions in lava surface morphology during flow (Cashman *et al.*, 1999; Polacci *et al.*, 1999; Soule *et al.*, 2004).

Groundmass crystals can form as a result of two processes—magma degassing and magma cooling. Shallow, decompression-induced degassing of water from the magma rapidly undercools the melt, promoting groundmass crystallization (e.g. Sparks & Pinkerton, 1978). The crystals might form in the rising magma (e.g. Métrich *et al.*, 2001; Melnik & Sparks, 2002) or, with a time delay, in the erupted lava flows (Lipman *et al.*, 1985). Radiative heat losses during lava flow at the surface can further increase the amount of groundmass crystals in the fluid lava (e.g. Kilburn, 1990; Crisp & Baloga, 1990; Cashman *et al.*, 1999; Harris *et al.*, 2005). This might induce rheological changes (Soule & Cashman, 2005), affecting the mode and rates of lava emplacement (e.g. Soule *et al.*, 2004). Strong links therefore exist between the concentration and distribution of crystals in fluid lava (as seen in the texture of quenched products), the gas and thermal budgets of the magma and lava upon eruption, and the lava rheology and surface morphologies. The groundmass textures of volcanic rocks thus provide key information on eruption dynamics and volcanic processes.

In this study, we address the relative importance of degassing and cooling on the crystallization, viscosity and thus rheology of lava produced by a well-known major basaltic eruption, the 8 months long AD 1783–1784 Laki eruption in Iceland (e.g. Thordarson & Self, 1993). The total volume of Laki products is 15·1 km^3 and lava is (14·7 km^3) in the form of lava. Guilbaud *et al.* (2005) showed that the flow surfaces underwent repetitive crust disruption during emplacement to produce rubbly pāhoehoe.

This study is based on a comparative petrological and compositional study of pumiceous tephra clasts and surface lava samples produced at different stages of the Laki eruption, as inferred from historical data and field relationships. The samples studied are glassy and were rapidly quenched, representing the magma and lava in a liquid state. In particular, glassy lava selvages (outer centimetre of lava surface) preserve the properties of the fluid lava core when it broke out at the surface. The combined whole-rock, crystal and matrix glass compositional data, together with textural and modal data and models of mineral–liquid equilibria, are used to trace the evolution of the Laki magma and lava upon eruption and emplacement. This study addresses the thermal efficiency of fluid lava transport within the flows and the role of groundmass crystallization on the formation of rubbly surface morphologies. We finally discuss the roles of degassing and cooling on the mode of lava emplacement during the Laki eruption.

THE LAKI ERUPTION: BACKGROUND

The Laki eruption is thought to have been part of a 2 year volcano-tectonic event at the Grímsvötn volcanic system in the Eastern Volcanic Zone of south Iceland (Fig. 1; Thordarson & Self, 1993, and references therein). It created a fissure system of 27 km length from which 15·1 km^3 of homogeneous quartz-tholeiite magma was erupted (Grönvold, 1984; Sigmarsson *et al.*, 1991; Thordarson & Self, 1993). Studies of contemporary accounts and tephra deposits provide us with a framework for the eruption dynamics (Thordarson & Self, 1993). The eruption can be divided into 10 eruptive episodes. Each episode was preceded by increasing seismic activity and characterized by the opening of a new fissure segment. The fissure segments opened from SW to NE, following the direction of the main rift zone. Eruptive intensity and lava production rates progressively decreased during each episode and over the course of the eruption. Lava fountains are thought to have reached a height of 1400 m during the initial episodes (I–II), with a mean height of 300–600 m (Thordarson & Self, 1993). Magma discharge rates peaked at about 6600 m^3/s during the opening of fissure 3 (Thordarson & Self, 1993). For the purpose of this study we divide each episode into four main eruptive phases (Fig. 2): (1) an initial, vent-clearing strombolian to subplinian explosive phase (EP) releasing large amounts of gas (Thordarson *et al.*, 1996) and depositing thick tephra fallout layers; (2) high-effusion-rate, high-fountaining phase (HF) delivering lava to the coast, forming the branches of Eldhraun and Brunahraun (Fig. 1b); (3) a low-fountaining phase (LF) emplacing short and gas-rich lava flows in proximal areas; (4) a final cone-building phase (CO) building numerous spatter–scoria cones and covering the highland valleys with a pile of overlapping lava flows. Lava surface morphologies vary from shelly near to the vent, to spiny then slabby, and finally, rubbly along single flows emplaced at greater distances from the vent, depending on lava effusion rates and the local topography (Guilbaud *et al.*, 2005).

METHODS

Sampling

The samples analysed in this study were collected from locations marked in figures 1, 3 and 4 and listed in Table 1. Four lava samples were collected for the analysis of whole-rock composition from sections located at widely separated locations (Table 1, Fig. 1). These were taken from the lava

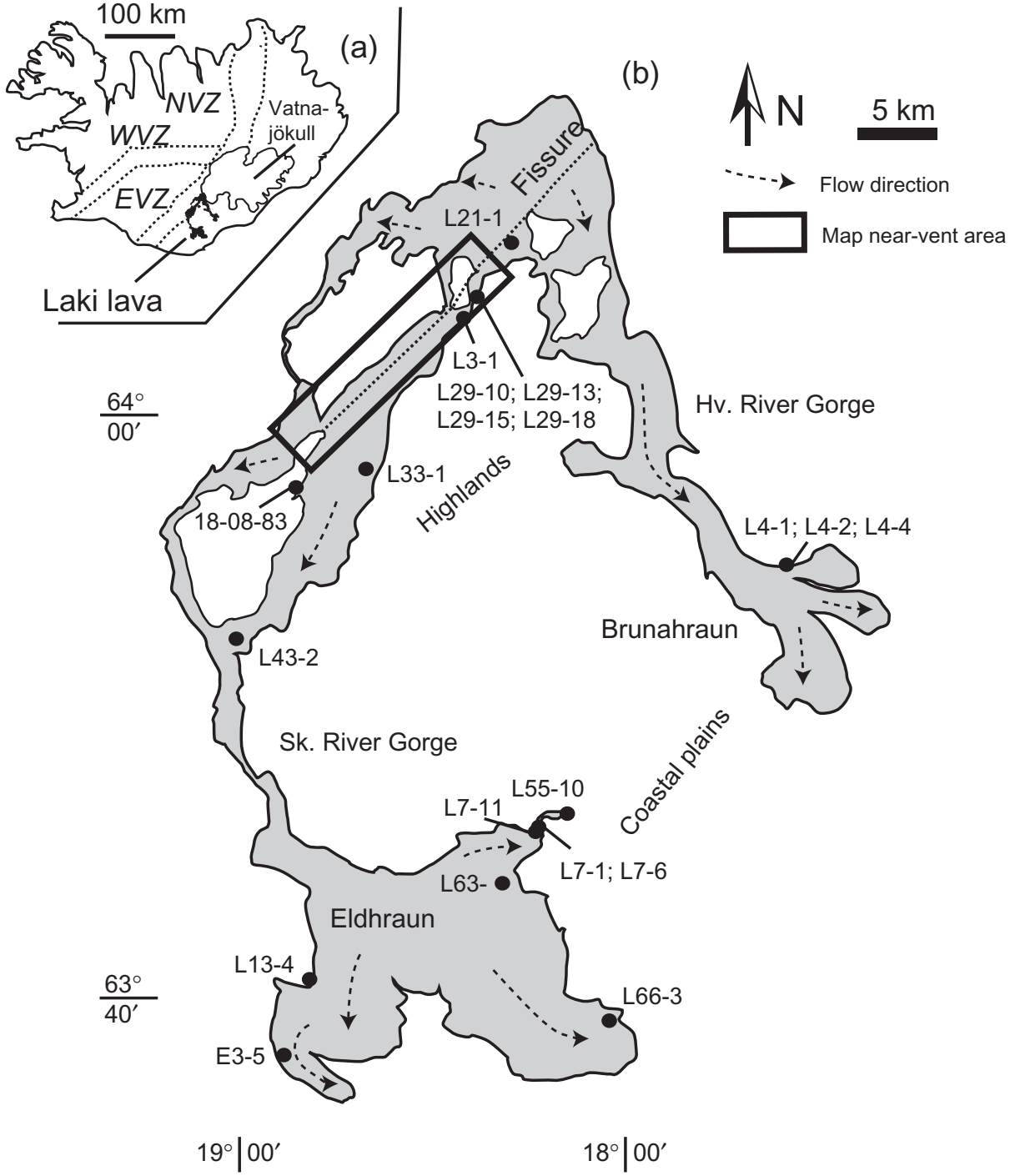

Fig. 1. (a) Location of Laki fissure and flow-field in Iceland. EVZ, NVZ and WVZ refer to approximate extent of Eastern, Northern and Western Volcanic Zones, respectively. (b) Map of Laki lava flow-field, showing location of lava samples analysed for glass and/or crystal compositions. Dashed lines with arrow indicate main flow direction. Sk., Skaftá, Hv., Hverfisfljót. Label L63- denotes location of samples starting with number L63- (see Fig. 4).

crust and core so as to limit the effects of post-emplacement alteration.

Tephra clasts were sampled from the proximal fall units identified and mapped by Thordarson & Self (1993). These units were produced during the early explosive phases of episodes I-II, III and V (see Table 1). Tephra comprise black scoria, achneliths, and glassy brown pumice lapilli (Thordarson & Self, 1993). In this study we selected small brown pumice clasts for detailed analysis. Their small size, high vesicularity and glassy texture

indicate that they were ejected at high speeds and quickly quenched at the margins of the explosive columns. They thus experienced minor cooling during flight. They are simply called tephra or vent tephra in the following discussion.

Glassy surface samples were collected at a variety of settings to study the influence of eruptive style, emplacement duration, and emplacement conditions on the characteristics of the fluid magma and lava. The most glassy outer part of the flows was selected to obtain homogeneous matrix glass for microprobe analysis, and to limit the effects of post-emplacement crystallization. Maps showing how the flow front advanced over time [see Thordarson *et al.* (2003) and Guilbaud *et al.* (2005, Fig. 8)] were used to infer the origin of each lava sample with respect to the eruptive sequence (Table 1). We mainly sampled products from the earliest, most productive, episodes of the eruption. Quenched lava samples are assumed to represent the fluid lava core as it reached the location of sampling. Samples were collected at proximal (near-vent), medial (highlands) and distal (coastal plains) locations from the fissure, from flows that can be related to high fountaining, low fountaining or cone-building activity along the fissure. We also collected sets of lava samples along single flows and from different surface morphologies. These sample sets are described as follows.

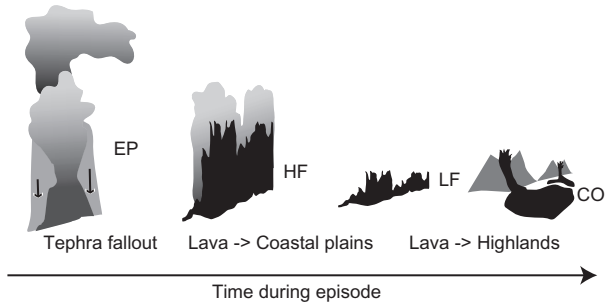

Fig. 2. Sketches representing the eruptive phases distinguished in this study: EP, explosive; HF, high fountaining; LF, low fountaining; CO, cone building. Transitions from one phase to another were gradational.

A first set of samples was collected along the length of flows <1 km long that are exposed in a narrow zone on the north side of the fissure, west of Mount Laki. These flows emerge in broad sheets from fissure segments, and later-formed cones, bombs and spatter rest on their proximal part. They have poorly disrupted surfaces, restricted hummocky margins, and proximal shelly (vesicle-rich) surfaces. Based on these characteristics, these flows are interpreted as products of low fountaining activity, at the transition between the high fountaining and cone-building phases (see above). They were called near-vent early formed flows by Guilbaud *et al.* (2005). Samples starting with number Ll7 were collected from such flows that issued from fissure 3, probably during episode III. Samples Ll4-3, Ll4-6 and Ll4-4 were collected along flows that issued from fissure 4 or 5 (these two segments overlap; see Thordarson & Self, 1993), and were thus probably produced during episode IV or V.

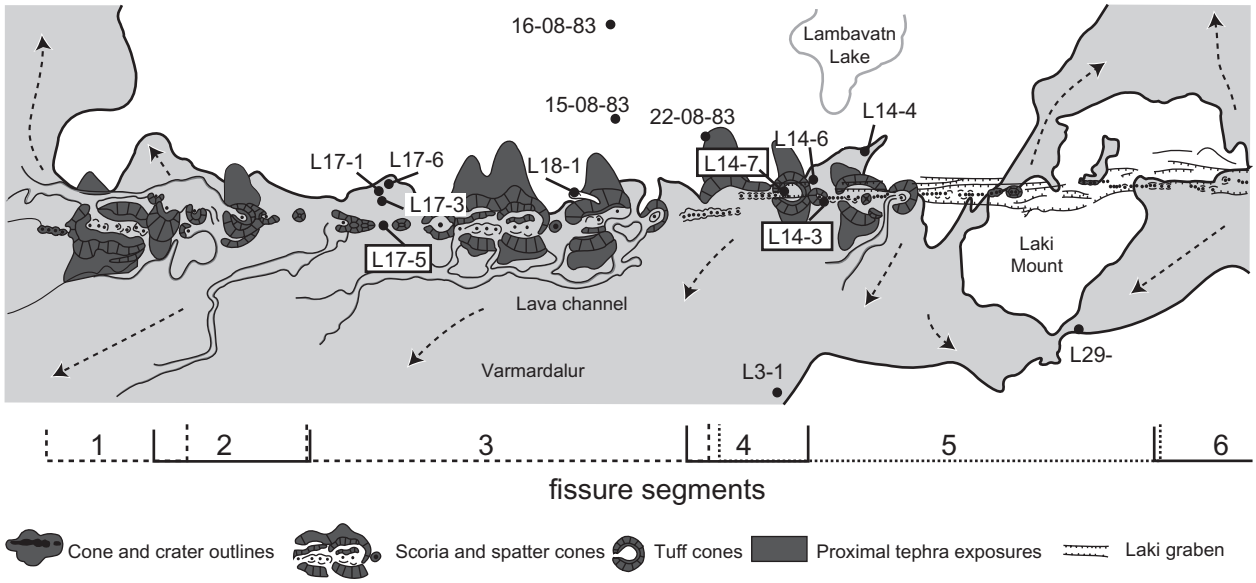

Fig. 3. Detailed map of near-vent area showing locations of tephra and near-vent lava samples. Domain in light grey represents lava. Dashed lines with arrow indicate main flow direction. Sample numbers in rectangles correspond to shelly pāhoehoe samples. Segments labelled 1–6 indicate extent of each identified fissure segment (see Thordarson & Self, 1993). Location of tephra sample 18-08-83 is shown in Fig. 1. Label L29- denotes location of samples starting with number L29-.

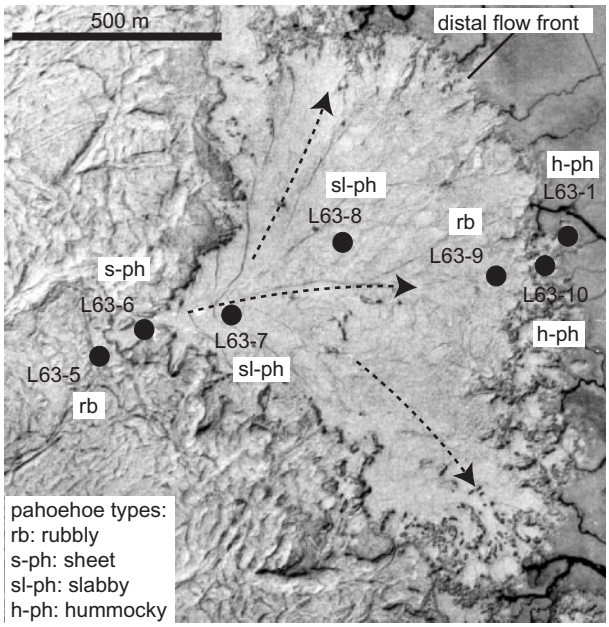

Fig. 4. Aerial photograph of the distal lava lobe on Eldhraun that was studied for down-flow compositional and textural variations, with location of samples collected (sample numbers starting L63-). Labels (rb, s-ph, etc.) denote surface morphology of lava where each sample was collected. Dashed lines with arrow indicate main flow direction.

A second set of samples was collected from short flows that were emplaced in proximal areas but were erupted in different conditions from the first set of samples. Sample L18-1 is from a minor lava flow that emerges from the top of a spatter cone built on fissure 3 and rests on its slopes. This flow might have been emitted late during episode III or during episode V when fissure segments 1–4 were active. A large phreatomagmatic cone formed in the initial phase of episode IV (P1 of Thordarson & Self, 1993). Sample L14-7 is from gas-rich lava located near a small spatter cone that formed in the centre of the phreatomagmatic cone. It might represent a late effusive phase of episode IV or an early phase of episode V, as fissure segments 4 and 5 overlap in time (Thordarson & Self, 1993). It is classified here as the product of a low fountaining phase because of its high vesicle content.

A third set of samples was collected at medial distance from the fissure (>2 km), on the highlands. Samples L3-1, L33-1 and L43-2 were collected from different types of surfaces along short, spiny to rubbly flows that bank against early formed rootless cone fields. These represent late CO phases of episode III or V. Samples starting with number L29- were collected at the margins of a lava flow of 2 km length that issued from fissure 6, along a sequence of 20–60 m long connected lobes. These lobes might have formed during the initial phase of episode VI. Tephra sample L21-1 was collected from a large field of rootless cones formed at an early stage of episode VI as a result of lava interacting with wet sediments. It is referred to as rootless cone tephra in the following discussion, to distinguish it from vent tephra samples.

A final set of samples was collected at the margins of the flow-fields on the coastal plains. Samples E3-5, L7-1, L7-11, L55-10 and L66-3 were collected from spiny-surfaced hummocky flows bordering the Eldhraun branch. Sample L66-3 is from the distal front of a lava branch emplaced by a major surge during episode III (23–24 June 1783). The other samples are from flows emplaced during episode V (1–20 July 1783) (see Guilbaud *et al.*, 2005, Fig. 8d). Samples with numbers starting with L63- were collected along a distal lava lobe of ~1 km length that probably formed during episode V (Fig. 4). As is characteristic of many other lobes in the flow-field, the lava surface on this lobe grades down-flow from smooth and coherent, to slabby, and then to rubbly, with sequences of spiny pāhoehoe lobes branching at the front (Fig. 4). Samples from all of these distinct types of lava surfaces were collected, and they represent lava that was quenched at different times along the active flow front as the flow advanced. Samples L4-2 and L4-1 were collected at the margin of a Brunahraun lava sub-branch, from inflated spiny-surfaced lobes. This lava branch mainly formed during episode VII (1–10 September 1783).

Textural analysis

In thin-section, lava surface samples typically display an outer brown glassy selvage grading into an opaque, microcrystalline zone (see Oze & Winter, 2005). Glass analyses were made on the outer selvage as they preserve clear glass representative of the liquid lava. We first analysed whole thin-sections of a few lava samples using a point counter, to assess the relative proportions of phenocrysts, groundmass crystals and vesicles in the lava. Backscattered electron (BSE) images of the outer selvages of a large set of samples were then taken using a microprobe, to determine more precisely the abundance and mode of groundmass crystals in tephra and lava, and vesicle content in tephra. The images were taken at a resolution of 4 μm/pixel. The edges of the photographs were cropped out as they showed evidence of image distortion. The software Scion Image (NIH version for PC) was used to scale the images and select the area covered by each mineral phase, using their difference in grey tones. The area covered by vesicles was extracted from the final results. This method is particularly well suited for plagioclase because this mineral displays a very distinct dark tone on the images. It is less precise for clinopyroxene and olivine, which show some overlap in the light grey range and display internal zoning. This resulted in some uncertainty in the measurement, which can be estimated as ±5 vol. %. We analysed an average of 10 images per sample to limit the effect of

Table 1: List of samples analysed with number and type of analyses completed

Sample	*D* (km)	Fissure	Episode	Phase	Lava surface type	Number of analyses done					
						H_2O	W-R	Crystals			Glass
								Pl	Ol	Cpx	
Lava interior											
L13-4 (core)							1				
L3-1 (crust)							1				
L4-4 (crust)							1				
L7-6 (core)							1				
Vent tephra											
15-08-83		3	III	EP							11
16-08-83		1–5	V	EP		1					5
18-08-83		1	I-II	EP		4		65	8	61	10
22-08-83		3	III	EP				89	6	22	10
Lava selvages											
Proximal (near-vent)											
L14-3	0·05	4/5	IV(V?)	LF	shelly						6
L14-6	0·2	4/5	IV(V?)	LF	spiny sheet	3		103	80	34	5
L14-7	0·05	4/5	IV(V?)	LF	shelly						4
L17-1	0·25	3	III	LF	spiny sheet			195	22	50	7
L17-3	0·1	3	III	LF	spiny sheet						5
L18-1	0·08	3	III(V?)	CO	spiny hcky	7		80	86		8
Medial (highlands)											
L3-1	3	4/5	IV(V?)	CO	spiny hcky			55	10	11	
L29-10	2	6	IV	CO	spiny hcky			1	8	15	
L29-13	2	6	IV	CO	spiny hcky						6
L29-15	2	6	IV	CO	spiny hcky						9
L29-18	2	6	IV	CO	spiny hcky						7
L33-1	6	3–5?	III(V?)	CO	spiny sheet						5
L43-2	20	3–5?	III(V?)	CO	slabby	1					7
L21-1*	0.5	6	VI	HF	*			129	34	17	7
Distal (coastal plains)											
L4-2	30	7	VII	HF	spiny hcky			187	67	46	10
E3-5	45	1–5	V	HF	spiny hcky			50	24	24	5
L7-1	50	1–5	V	HF	spiny hcky			175	223	159	
L7-11	50	1–5	V	HF	spiny hcky			24	11	12	
L55-10	54	1–5	V	HF	spiny hcky						9
L63-10	49	5	V	HF	spiny hcky						9
L63-1	49	5	V	HF	spiny hcky						6
L63-5	48	5	V	HF	rubbly						5
L63-6	48	5	V	HF	spiny sheet						4
L63-7	48	5	V	HF	slabby			34	39	14	5
L63-8	48	5	V	HF	slabby						8

(continued)

Table 1: Continued

Sample	*D* (km)	Fissure	Episode	Phase	Lava surface type	Number of analyses done					
						H_2O	W-R	Crystals			Glass
								Pl	Ol	Cpx	
L63-9	48	5	V	HF	rubbly			15	14		14
L66-3	60	3	III	HF	spiny hcky			29	17		7
Total						19	4	1248	656	453	207

*Sample of rootless cone tephra.
D, distance from the vent. Surface type: hcky, hummocky. Compositional data: W-R, whole-rock (XRF); H_2O, analysis by FTIR of dissolved total water in matrix glasses; Pl, plagioclase; Ol, olivine; Cpx, clinopyroxene; Glass, analysis of major elements in matrix glasses by EMPA (see text). Sampling location of tephra samples: 15-08-83, Unit S2, section 98, Eystrisker; 16-08-83, Unit S3, section 114, Vikradalur; 18-08-83, Unit S1, section 144, Hnuta; 22-08-83, Unit S2, section 94, Eystrisker (see Thordarson & Self, 1993). Fissure, Episode, Phase: inferred eruptive activity along the fissure during quenching of sample. Phases: EP, explosive; HF, high-fountaining; LF, low-fountaining; CO, cone-building (see text).

these uncertainties. In general, we observed that natural textural variations within single samples were larger than those induced by uncertainties in the method. In particular, clinopyroxene crystals commonly cluster, which causes large standard variations in the measurements of this phase on BSE images (see Results section).

Crystal number densities and sizes were quantified on BSE images for a small set of tephra and lava samples. Samples were selected to cover the whole range in total groundmass crystal content. We used the hand-tool of Scion Image to measure the width and length of each distinguishable crystal on the previously scaled images. The minimum measurable dimension can be considered to be 10 μm (~2 pixels). The total area of analysis was chosen so as to obtain the dimensions of a large number of crystals. More than 300 plagioclase crystals per sample were analysed so as to obtain representative data and account for textural variability. Crystals were measured in a consistent manner, to allow reliable comparison between samples. For example, we systematically considered the plagioclase laths that form parallel to branching clusters as separate entities. Clinopyroxene crystal sizes were not measured because of their strong clustering, which makes them difficult to identify individually.

Whole-rock, glass and crystal compositions

Whole-rock data were obtained by X-ray fluorescence spectrometry (XRF) using an ARL Fisons wavelength-dispersive XRF system. Analyses were carried out using fused glass discs and pressed pellets, following a procedure routinely used at the Open University. An assessment of the precision of the method has been presented by Ramsey *et al.* (1995). Data on crystal and matrix glass compositions were obtained at the Open University by electron microprobe analysis (EMPA) using a Cameca SX100 electron microprobe. We used a 20 kV accelerating voltage, a 20 nA beam current, and a beam size of 5 μm for crystals and 20 μm for matrix glasses. Traverses across crystal–glass interfaces were collected using a 10 μm beam. The reproducibility of microprobe analyses of crystals can be estimated as ±2 mol % in An, Fo, and Wo for plagioclase, olivine, and clinopyroxene, respectively. For matrix glass analysis, a maximum of 10 consecutive analyses was carried out during each run. Several points were analysed in each sample to assess the homogeneity of the matrix glass and detect anomalous analyses of microcrystalline areas. Na was analysed first, using a short counting time, to minimize loss by volatilization. Glass standard BHVO-2 was analysed at the beginning and end of each run. The standard deviation of those replicate analyses for each element was taken as an estimation of analytical uncertainties and is <0·2% for most elements (Table 2). For example, the standard deviations are ~0·1 wt % for MgO, 0·12 wt % for CaO, and 0·13 wt % for FeO. The uncertainty is slightly higher for SiO_2 (0·4%) and for minor elements such as K_2O, Na_2O and P_2O_5. Mean values recommended by the US Geological Survey (USGS) are close to those measured in this study (Table 2) apart from those for SiO_2 and CaO (SiO_2 is higher by 0·5 wt % and CaO lower by 0·2 wt % compared with the recommended values), which can be due to different operating conditions. These deviations do not affect the interpretation of the data collected in this study, as they are internally consistent.

Water content of matrix glasses

The H_2O content of the glass of selected tephra and glassy lava selvages was measured on doubly polished wafers by Fourier-transform infrared spectrometry (FTIR), using a Thermo Nicolet Nexus FTIR system coupled with

a Continuμm IR microscope. Standard EverGlo mid-IR source optics, a Ge-on-KBr beamsplitter, and a MCT-A detector (11700–750 cm^{-1}) were used. The aperture was positioned so as to analyse patches of clear brown glass as far as possible from crystals, vesicles, microcrystalline areas (effect of post-emplacement cooling), and areas previously analysed by EMPA. Several points were analysed on each wafer, to assess the internal homogeneity of the glasses and detect anomalous analyses of crystalline glass. The Beer–Lambert law was applied to derive the total water content ($H_2O_{mol} + OH^-$) from the resulting spectra, following the method explained by Stolper (1982). In the samples analysed, water was only dissolved as hydroxyl groups (OH^-), with an absence of the characteristic peak of molecular water (H_2O_{mol}) at ~1630 cm^{-1}. This is a feature often observed in basaltic glasses with low water contents (Dixon *et al.*, 1988, 1995). The Beer Lambert law is expressed as $C = aw/(\varepsilon\rho d)$, where C is the total water content, a is the intensity of the broad asymmetric peak measured graphically at ~3530–3550 cm^{-1} (OH stretching vibration; see Scholze, 1959), w the molecular mass of H_2O (18·02 g/mol), ε s the molar absorption coefficient (61 L/mol per cm, after Dixon *et al.*, 1988), and ρ is the glass density (2·75 ± 0·1 g/cm^3, taken from Métrich *et al.*, 1991). The thickness d of the sample was measured with a Mitutoyo Digimatic Indicator micrometer with ±3 μm uncertainty. Uncertainties as a result of inaccuracies in the determination of molar coefficients and the limitation of the background method are typically ~10% (Dixon *et al.*, 1988).

Table 2: Average composition of repeated analyses of glass standard BHVO-2 and recommended values

	This study		USGS*
	Average	SD	
SiO_2	50·42	0·401	49·90
TiO_2	2·75	0·045	2·73
Al_2O_3	13·54	0·164	13·50
FeO	11·02	0·131	11·07
MnO	0·17	0·010	0·17
MgO	7·24	0·095	7·23
CaO	11·21	0·123	11·40
Na_2O	2·20	0·062	2·22
K_2O	0·51	0·014	0·52
P_2O_5	0·28	0·018	0·27
Total	99·32	0·518	99·01

SD, standard deviation.
*Recommended values for BHVO-2 taken from http://minerals.cr.usgs.gov/geo_chem_stand/index.html.

RESULTS

Whole-rock analysis

The bulk lava samples analysed in this study by XRF have a restricted range in major element concentrations (50·41 ± 0·17 SiO_2 wt %; 5·75 ± 0.01 MgO wt %, Table 3). This range is in agreement with other bulk-rock analyses carried out by inductively coupled plasma mass spectrometry (ICP-MS) on a larger set of samples (Thordarson *et al.*, 1996; T. Thordarson, unpublished data). The sample set used in those studies included tephra samples from the same units as those analysed in this study, and showed that tephra and lava samples had similar bulk-rock compositions. Together, these data confirm the whole-rock homogeneity of the products from the Laki eruption (see also Grönvold, 1984; Sigmarsson *et al.*, 1991).

Crystal morphologies and compositions

General description

We distinguish two main types of crystals in the samples: (1) phenocrysts, which are made of >100 μm plagioclase, >300 μm clinopyroxene and >500 μm olivine; (2) groundmass crystals, which are made of the same mineral phases with smaller sizes.

Phenocrysts mainly occur as 2–3 mm glomerophyric clusters. These are made of complex intergrowths of large tabular plagioclases enclosing smaller round-shaped crystals (Fig. 5a), with minor amounts of olivine and clinopyroxene. The few olivine and clinopyroxene phenocrysts found during this study displayed oval and prismatic shapes, respectively. Many phenocrysts contain glass inclusions. They can be located at the centre of the crystal (see below) but, most often, they occur at crystal

Table 3: Normalized XRF whole-rock analysis of lava samples from flow interiors

	Sample				Average
	L13-4	L3-1	L4-4	L7-6	
SiO_2	50·11	50·16	50·16	50·11	50·14 (0·030)
TiO_2	2·76	2·80	2·73	2·80	2·77 (0·035)
Al_2O_3	13·82	13·77	13·96	13·71	13·81 (0·106)
FeO	13·55	13·70	13·31	13·64	13·55 (0·172)
MnO	0·23	0·23	0·22	0·23	0·22 (0·004)
MgO	5·71	5·71	5·76	5·72	5·72 (0·022)
CaO	10·41	10·36	10·45	10·35	10·39 (0·046)
Na_2O	2·70	2·56	2·70	2·72	2·67 (0·073)
K_2O	0·43	0·41	0·41	0·43	0·42 (0·010)
P_2O_5	0·30	0·30	0·30	0·30	0·30 (0·002)

Major elements in wt %. Average reported with standard deviation in parentheses.

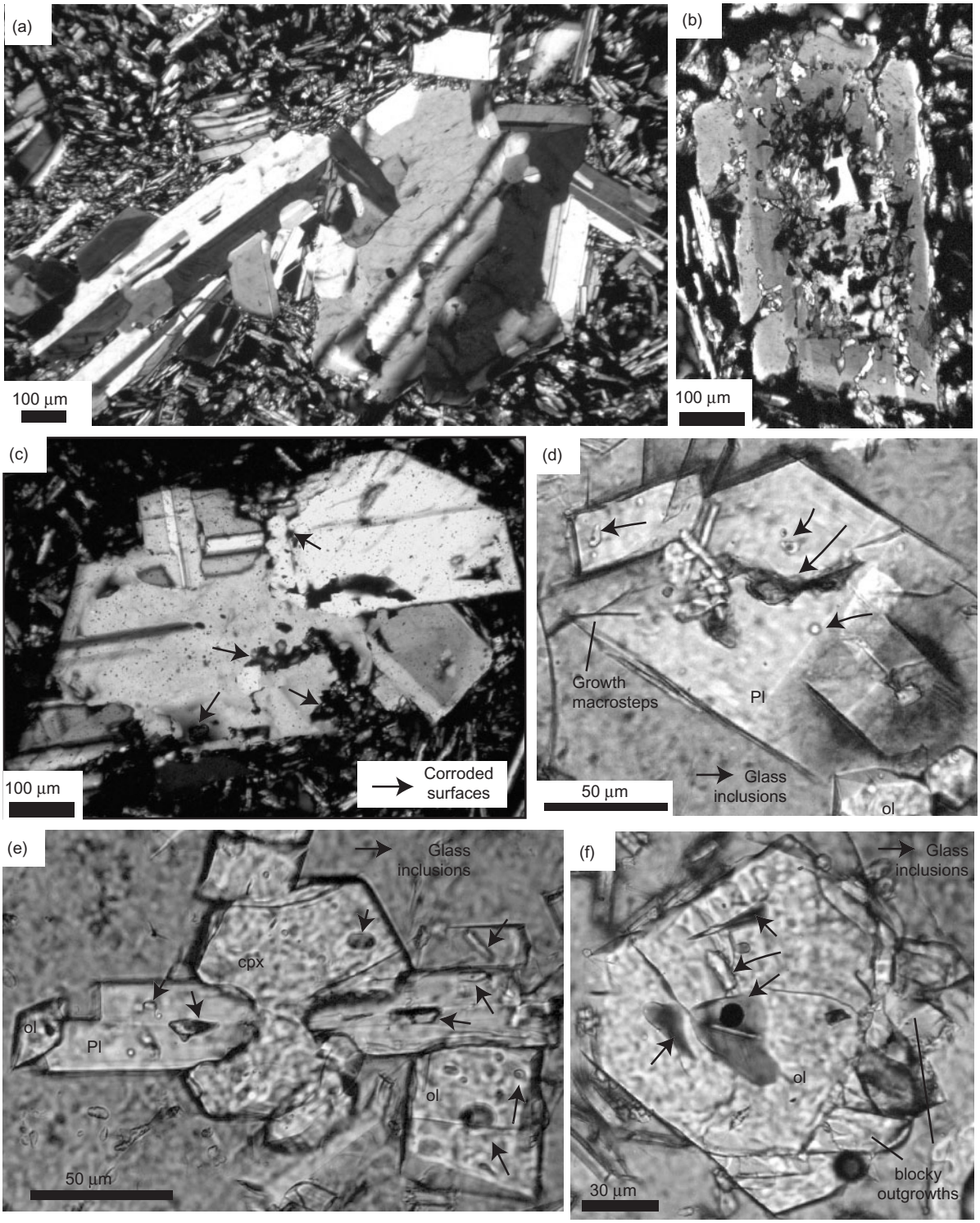

Fig. 5. Textural characteristics of crystals seen by optical microscopy. (a–c) Photomicrographs in cross-polarized light; (d–f) photomicrographs in plane-polarized light (plag, plagioclase; cpx, clinopyroxene; ol, olivine). (a) Typical plagioclase phenocryst cluster. Sample L7-5 (collected at same location as sample L7-1 from flow core). (b) Individual plagioclase phenocryst with irregular, corroded rims and abundant glass inclusions in centre. Sample L7-5 [see caption for (a)]. (c) Plagioclase phenocryst cluster with corroded rims. Sample L7-11. (d) Groundmass plagioclase forming tablets with inclusions of matrix glass and tiny groundmass crystals. The macrosteps along crystal faces should be noted (see Kirkpatrick, 1981, fig. 40). Sample L14-6. (e) Intergrowth of groundmass crystals of plagioclase, clinopyroxene and olivine with abundant glass inclusions. Sample L14-6. (f) Arrow-shaped groundmass olivine showing melt inclusions with boundaries parallel to outer crystal faces, and blocky outgrowths. Sample L17-3.

rims, where they are abundant, <20 μm across and elongated parallel to the outer crystal faces. Some plagioclases display corroded outer faces overgrown by tiny groundmass crystals (Figs 5b and c).

Groundmass crystals are dispersed in the matrix glass or attached to the rim of phenocrysts. They have anhedral to subhedral shapes and some have skeletal morphologies and abundant glass inclusions (Figs 5d–f). Plagioclase groundmass crystals mainly form high aspect ratio laths branched in parallel. They often show outgrowths <10 μm long that form V-shaped swallowtail ends. Some crystals display a distinct tablet shape and contain abundant inclusions of matrix glass and tiny granular crystals (Fig. 5d). Crystal faces commonly show macrosteps (Fig. 5d) and teeth-like irregularities. Clinopyroxene groundmass crystals are round to prismatic in shape. They range from granular crystals that are barely seen using an optical microscope to large crystal aggregates up to 200 μm across. They are often intergrown with radiating laths of plagioclase (Fig. 5e). Olivine groundmass crystals are round to prismatic, and often display round to irregular-shaped inclusions and blocky outgrowths (Fig. 5f).

Crystal compositional ranges

Figure 6 shows the results from electron microprobe analysis of minerals, expressed as a function of the cation percentage An^* $[100 \times Ca/(Ca + Na)]$ for plagioclase, En^* $[100 \times Mg/(Mg + Fe)]$ for clinopyroxene and Fo $[100 \times Mg/(Mg + Fe)]$ for olivine. Representative crystal compositions are reported in Table 4.

Phenocrysts have a wide range in composition. They contain cores that are compositionally more primitive ($An^*_{>70}$; $Fo_{>75}$; $En^*_{>78}$) than the crystal borders, which are similar in composition to groundmass crystals (Fig. 6). Some phenocrysts contain strongly corroded, primitive cores that cover the range $An^*_{82–91}$ in plagioclase (xeno core in Fig. 6; see below). They were interpreted as xenocrysts assimilated in the Laki magma at depth (Métrich *et al.*, 1991; Bindeman *et al.*, 2006). Groundmass crystals are distinctly less evolved in tephra ($An^*_{58–67}$; $Fo_{72–78}$; $En^*_{72–81}$) than in lava selvages ($An^*_{49–70}$; $Fo_{63–78}$; $En^*_{57–78}$) (Fig. 6). There is a general negative correlation between the size of the crystals and the degree of compositional evolution of their core. We note that some plagioclase groundmass crystals (i.e. <100 μm) contain round-shaped primitive cores (e.g. $An^*_{>70}$) that are thought to be broken pieces of crystals that were originally part of larger phenocryst clusters. These crystals were considered as phenocrysts in the analysis.

Crystal zoning

Plagioclase phenocrysts are generally formed of two zones: an An^*-rich core ($An^*_{70–82}$) and an An^*-poor mantle ($An^*_{60–70}$) that is sometimes overgrown by a thin, more evolved rim (Fig. 6). In high-contrast BSE images, the An^*-rich core forms a light grey zone with a diffuse rounded outline, overgrown by a darker An^*-poor zone bounded by straight faces and best developed at crystal edges (Figs 7a and b). Both cores and mantles display fine oscillatory zoning in the range ±2 mol % An^* on which larger-scale variations are superimposed (±5 mol % An^*) (Fig. 7a). The core–mantle transition is typically sharp, forming an An^* gap in profiles (profile A–B in Fig. 7a). This gap ranged from $\Delta An^* = 8\%$ to $\Delta An^* = 13\%$ in the profiles studied. In rarer cases, this transition was more gradational, occurring across a 10–20 μm wide zone. Some phenocrysts contain irregularly zoned cores, commonly associated with the presence of large internal glass inclusions (Fig. 7b).

When present, xenocryst cores in plagioclase phenocrysts form a distinct light-coloured zone on BSE images bordered by an irregular outline, which define a zone with distinctly higher An^* than the overgrown 'normal' core (Fig. 7c). In one case, a strongly irregular zone with abundant glass inclusions marked the limit of the xenocryst core with the 'normal' core (Fig. 7d).

Plagioclase groundmass crystals typically contain homogeneous, oscillatory-zoned cores covering the range $An^*_{64–70}$ overgrown by thin, more evolved rims. In one case, reverse zoning was detected across the rim. Some crystals display irregular oscillatory zoning in bands parallel to the outer faces. This is sometimes associated with the presence of abundant glass inclusions in the crystal (Fig. 7e).

Clinopyroxene crystals are either normally zoned with homogeneous core compositions and a drop in En^* content at the outermost rim, or irregularly zoned in bands parallel to the outer face, in sectors, or in irregular patches (Figs 8a and b).

Olivine phenocrysts are composed of homogeneous cores in the range $Fo_{72–81}$ overgrown by normally zoned rims that extend to groundmass crystal compositions (Fig. 8c). The largest groundmass crystals (>100 μm) are composed of an unzoned core in the range $Fo_{69–78}$ with a sharp drop in Fo content at the rim. Smaller crystals have cores <Fo_{69} and no detectable zoning.

Textural analysis

The tephra and lava samples are texturally distinct in terms of vesicularity and groundmass crystal content (Fig. 9). The tephra contain high amounts of densely distributed well-rounded vesicles, which vary greatly in abundance between different clasts (>40 vol. %, Table 5 legend). In lava selvages, vesicles are less abundant (15–40 vol. %, Table 6), less numerous, more irregular in shape and often larger sized. Crystal abundance data were recalculated on a vesicle-free basis and are quoted as such below. The abundance of phenocrysts is similarly low in tephra (1–10 vol. %, Thordarson *et al.*, 1996) and lava surface samples (0–7 vol. %, Table 6), and they are

Table 4: Representative crystal compositions

	Plagioclase				Clinopyroxene					Olivine			
Crystal type:	ph	ph	ph	xeno	gdm	gdm	ph	ph	xeno	gdm	gdm	ph	xeno
Analysis location:	rim	mantle	core	core	rim	core	core	rim	core	rim	core	core	core
Sample:	L18-1	L18-1	L18-1	L18-1	L4-2	L17-1	L7-1	L7-1	L7-5	L14-6	L14-6	L7-1	L7-1
SiO_2	54·16	52·22	50·14	46·52	50·15	50·42	51·43	51·55	52·63	37·51	37·79	38·05	39·04
TiO_2	–	–	–	–	1·65	1·22	0·96	1·23	0·77	0·08	0·05	0·00	0·00
Al_2O_3	28·78	29·35	31·55	33·78	3·17	3·49	2·94	2·15	2·10	0·03	0·05	0·00	0·03
Cr_2O_3	–	–	–	–	0·03	0·23	0·28	0·01	0·19	0·03	0·00	0·02	0·04
MgO	0·17	0·15	0·16	0·09	14·69	15·66	16·15	13·92	16·50	33·53	35·37	37·59	40·32
CaO	12·02	13·44	14·96	17·43	16·78	19·39	20·02	17·05	19·84	0·38	0·33	0·28	0·30
MnO	–	–	–	–	0·32	0·23	0·20	0·32	0·20	0·38	0·38	0·33	0·30
FeO	0·78	0·83	0·74	0·62	12·65	9·08	8·12	13·54	7·88	28·88	26·94	23·33	19·47
NiO	–	–	–	–	0·01	0·01	0·02	0·01	0·02	0·06	0·08	0·11	0·14
Na_2O	4·41	3·84	2·84	1·44	0·31	0·31	0·30	0·29	0·24	0·02	0·01	0·00	0·00
K_2O	0·13	0·08	0·05	0·03	0·00	0·01	0·00	0·01	0·00	0·00	0·00	0·00	0·00
Total	100·45	99·91	100·44	99·91	99·76	100·04	100·40	100·09	100·36	100·90	100·99	99·71	99·64
Formula													
Si	2·443	2·381	2·283	2·145	1·887	1·875	1·898	1·937	1·935	0·999	0·996	0·999	1·006
Ti	–	–	–	–	0·047	0·035	0·027	0·035	0·021	0·002	0·001	0·000	0·000
Al	1·530	1·577	1·693	1·835	0·141	0·153	0·128	0·095	0·092	0·001	0·002	0·000	0·001
Cr	–	–	–	–	0·002	0·006	0·008	0·000	0·006	0·001	0·000	0·000	0·001
Mg	0·012	0·010	0·011	0·006	0·824	0·869	0·888	0·780	0·905	1·332	1·390	1·471	1·549
Ca	0·581	0·657	0·730	0·861	0·677	0·773	0·792	0·687	0·782	0·011	0·009	0·008	0·008
Mn	–	–	–	–	0·011	0·008	0·006	0·011	0·006	0·009	0·008	0·007	0·007
Fe	0·029	0·032	0·028	0·024	0·398	0·282	0·251	0·426	0·242	0·643	0·594	0·512	0·419
Ni	–	–	–	–	0·000	0·000	0·000	0·000	0·000	0·001	0·002	0·002	0·003
Na	0·386	0·339	0·250	0·129	0·023	0·023	0·021	0·021	0·017	0·001	0·001	0·000	0·000
K	0·008	0·005	0·003	0·002	0·000	0·000	0·000	0·000	0·000	0·000	0·000	0·000	0·000

(continued)

Table 4: Continued

	Plagioclase				Clinopyroxene					Olivine			
Crystal type:	ph	ph	ph	xeno	gdm	gdm	ph	ph	xeno	gdm	gdm	ph	xeno
Analysis location:	rim	mantle	core	core	rim	core	core	rim	core	rim	core	core	core
Sample:	L18-1	L18-1	L18-1	L18-1	L4-2	L17-1	L7-1	L7-1	L7-5	L14-6	L14-6	L7-1	L7-1
Total	4·989	5·002	4·998	5·002	4·007	4·023	4·019	3·992	4·004	2·999	3·002	3·001	2·993
Cation ratio													
Fo										67·4	70·1	74·2	78·7
Wo					35·7	40·2	41·0	36·3	40·5				
En					44	45·2	46·0	41·2	46·9				
An	59·6	65·6	74·3	86·8									
Or	0·82	0·50	0·31	0·20									

Major elements in wt %. –, not analysed. Crystal type: xeno, xenocryst; ph, phenocryst; gdm, groundmass crystal. Formula based on eight oxygens for plagioclase, six oxygens for clinopyroxene, four oxygens for olivine.

sparsely distributed. Groundmass crystals are rare in tephra (4–7 vol. %, Table 5) but abundant in lava selvages (20–40 vol. %, Table 5). Plagioclase is the dominant crystal phase. Groundmass plagioclase varies in the range 15–25 vol. % in lava selvages, compared with 5–15 vol. % for clinopyroxene and 2–5 vol. % for olivine (Table 5). In the samples studied, plagioclase number density is in the range of 160–450 crystals/mm^2 in lava selvages, compared with ~20–52 crystals/mm^2 in tephra (Table 7). Olivine groundmass crystals are rare in tephra (<1·1 crystals/mm^2) and abundant in lava (20–140 crystals/mm^2) (Table 7). We note that in lava selvages, the number density of crystals varies inversely with their volumetric abundance.

Matrix glass compositions

Major element analyses of clear homogeneous glass in samples of the outer lava selvage were obtained by electron microprobe; the complete dataset is reported in an Electronic Appendix (available at http://www.petrology.oxfordjournals.org). Average compositions for repeated analyses in each sample are given in Tables 8 and 9, along with the associated standard deviations. The whole-rock and matrix glass data are aligned along a typical tholeiitic trend defined by, with decreasing MgO, increasing TiO_2, FeO, MnO, K_2O and P_2O_5, decreasing Al_2O_3 and CaO, and constant to slightly decreasing SiO_2 and Na_2O (see plot of TiO_2 vs MgO in Fig. 10). Tephra and lava glass data collected in this study are separated by a distinct gap in MgO (tephra: 5·4–5·6 wt % MgO, lava: 4·3–5·0 wt % MgO), and other correlated elements (Fig. 10, Tables 8 and 9). Thordarson *et al.* (1996) and T. Thordarson (unpublished data) analysed glasses from a larger number of tephra clasts displaying a wider range in vesicularity. Their glass data cover a slightly wider range (5·2–5·6 wt % MgO, Fig. 10) but do not bridge the compositional gap between tephra and lava glasses.

The range of samples analysed allows any temporal and spatial changes in glass (liquid) compositions of the products to be assessed. The range covered by tephra and lava samples does not show any significant variation depending on the eruptive episode considered (Fig. 11), apart from a slight increase in the degree of evolution of the liquid in tephra from episode VII (unit S4, ~5·2 wt % MgO; Thordarson *et al.*, 1996; T. Thordarson, unpublished data). Tephra produced from episodes I–V cluster in the range 5·3–5·6 wt % MgO, with a marked spread of data for each unit (Fig. 11). Glass composition weakly correlates with sample vesicularity according to Thordarson *et al.* (1996).

Lava produced by low fountaining (LF) activity have a systematically less evolved liquid composition (4·8–5·0 wt % MgO) than lava produced from earlier high fountaining (HF) phases and later cone-building (CO)

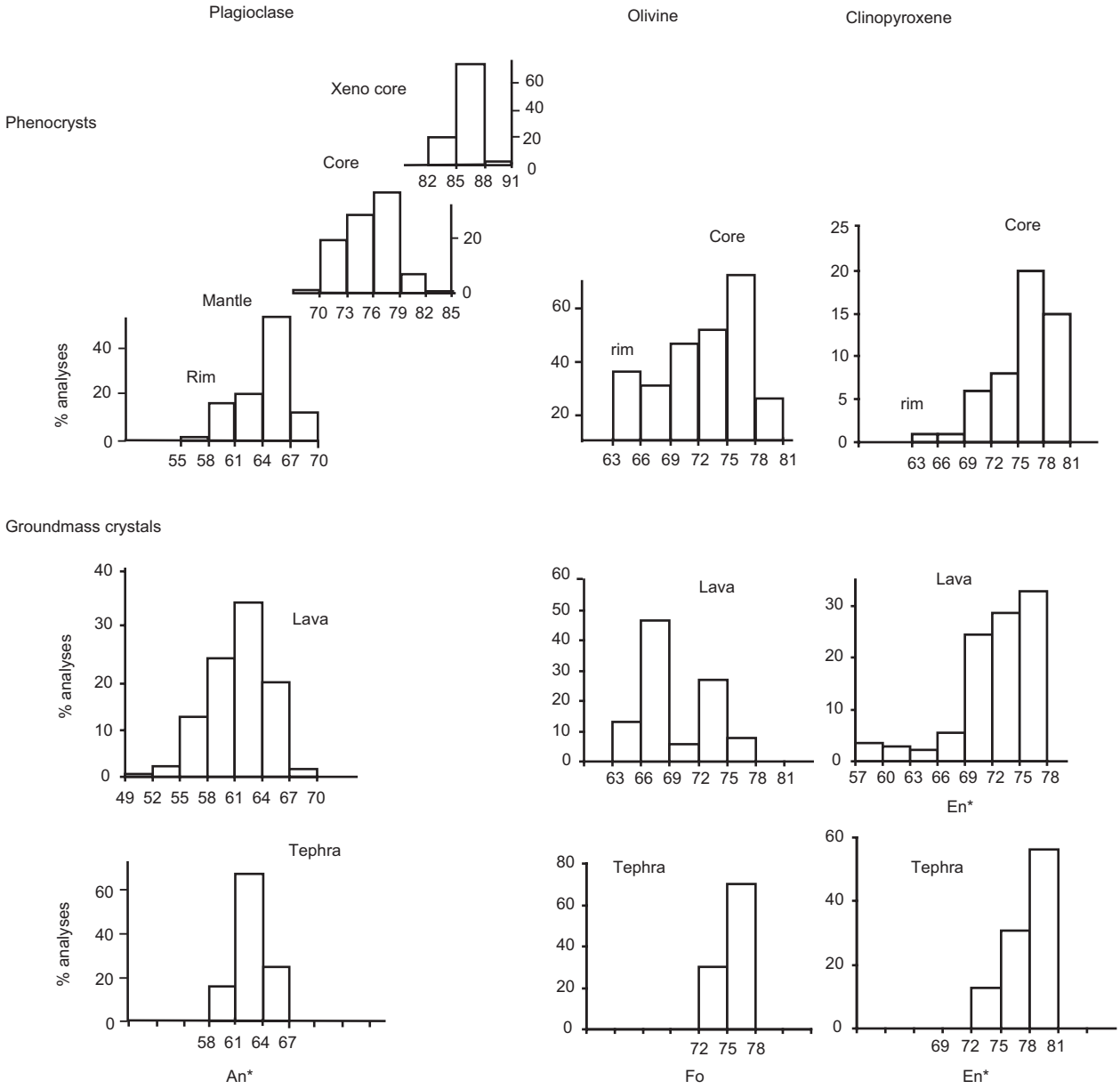

Fig. 6. Histograms of plagioclase, olivine and clinopyroxene compositions for phenocrysts in lava selvages and groundmass crystals in tephra and lava selvages. Vertical axes are percentage of analyses. The histogram labelled xeno core reports the range within a traverse across a xenocryst core in a plagioclase phenocryst cluster in sample L4-2.

phases, which cluster in the range 4·3–4·7 wt % MgO (Figs 10 and 11). The distance travelled by the lava from the vent was not the controlling factor, as samples collected from the highlands and the coastal plains have similar ranges of glass composition (Fig. 12). Sample L18-1, from a late cone outflow, has glass compositions that are distinctly more evolved (~4·41 wt % MgO) than those of lava produced by LF activity during the same episode and emplaced at similar distances from the vent (e.g. samples starting with number L17-: 4·8–5·0 wt % MgO).

Using the data available, we can estimate down-flow variations in the liquid composition of the fluid lava transported within the flows produced during HF phases. Glassy tephra from rootless cone fields on the highlands represent the fluid lava core that was quenched at proximal to medial distances from the vent as the flows covered water-saturated ground. The glass compositions of these samples [4·6–4·8 wt % MgO; see sample L21-1 here and further data given by Thordarson *et al.* (1996)] are similar to those of samples collected from distal breakouts on the coastal plain (e.g. sample L55-10 ~ 4·63 wt % MgO).

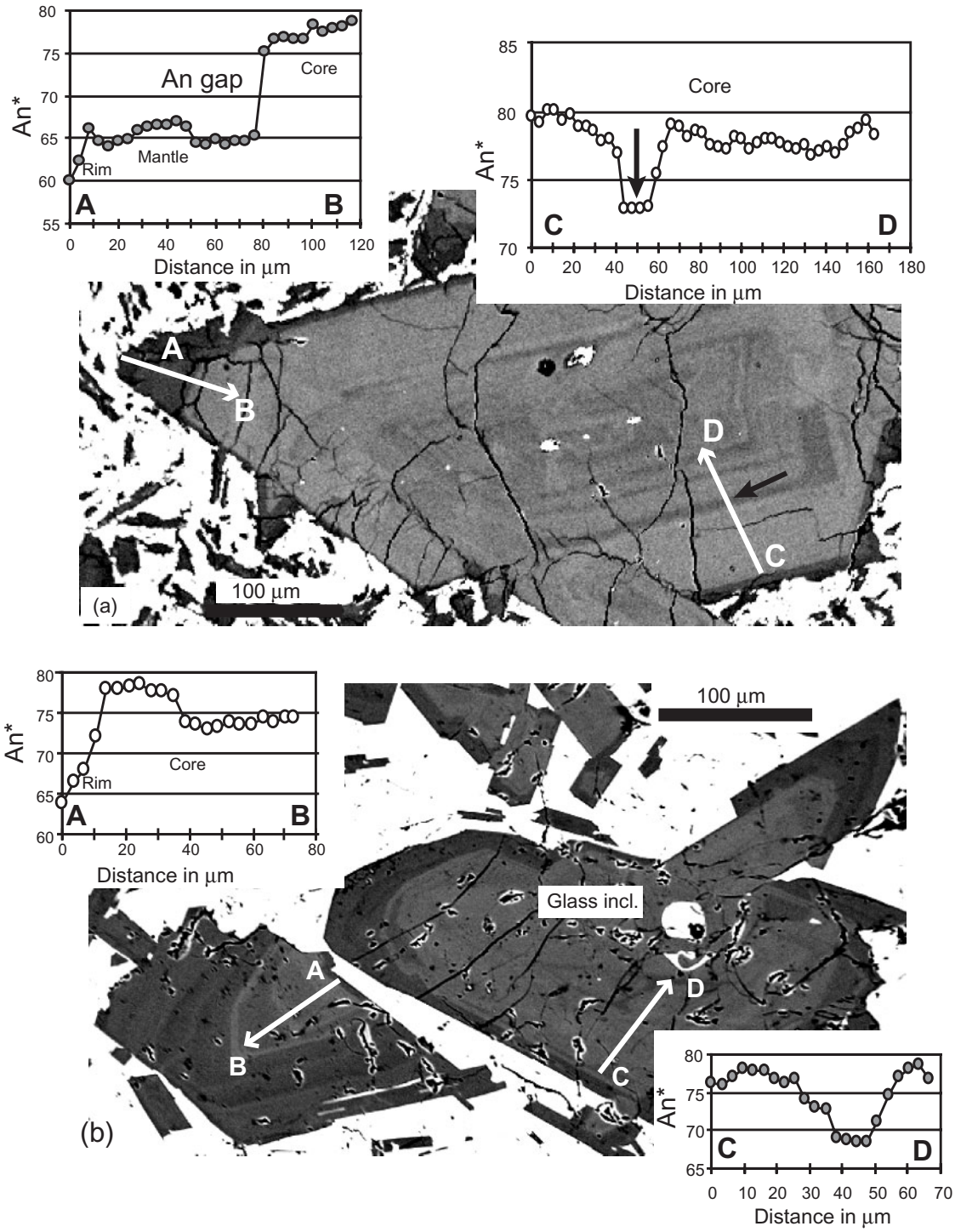

Fig. 7. Zoning in plagioclase: BSE images and corresponding electron microprobe profiles. (a) Typical plagioclase phenocryst showing oscillatory-zoned core (profile C–D) overgrown by An-poor mantle and rim (profile A–B). Sample L7-1. (b) Plagioclase phenocrysts showing patchy-zoned cores (profiles A–B and C–D) overgrown by lower-An rim. Large phenocryst displays glass inclusion in core. Colour banding in darker rim should be noted. Sample L14-6. (c) Phenocryst with rounded, irregular-shaped xenocryst core showing distinct high An content and fine oscillatory zoning. Rounded tiny groundmass olivines (gdm olivine in figure) are enclosed by An-poor darker mantle and rims. Sample L18-1. (d) Phenocryst with large xenocryst core. The wide irregularly zoned and glass-inclusion-rich boundary layer between high An xenocryst core and lower An phenocryst 'normal' core should be noted. Ranges in An* content measured by EMPA are reported in the figure. Sample L18-1 [same cluster as shown in (c)]. (e) Groundmass plagioclase with marked face-parallel irregular zoning at terminations and small abundant melt inclusions in centre. Sample L14-6.

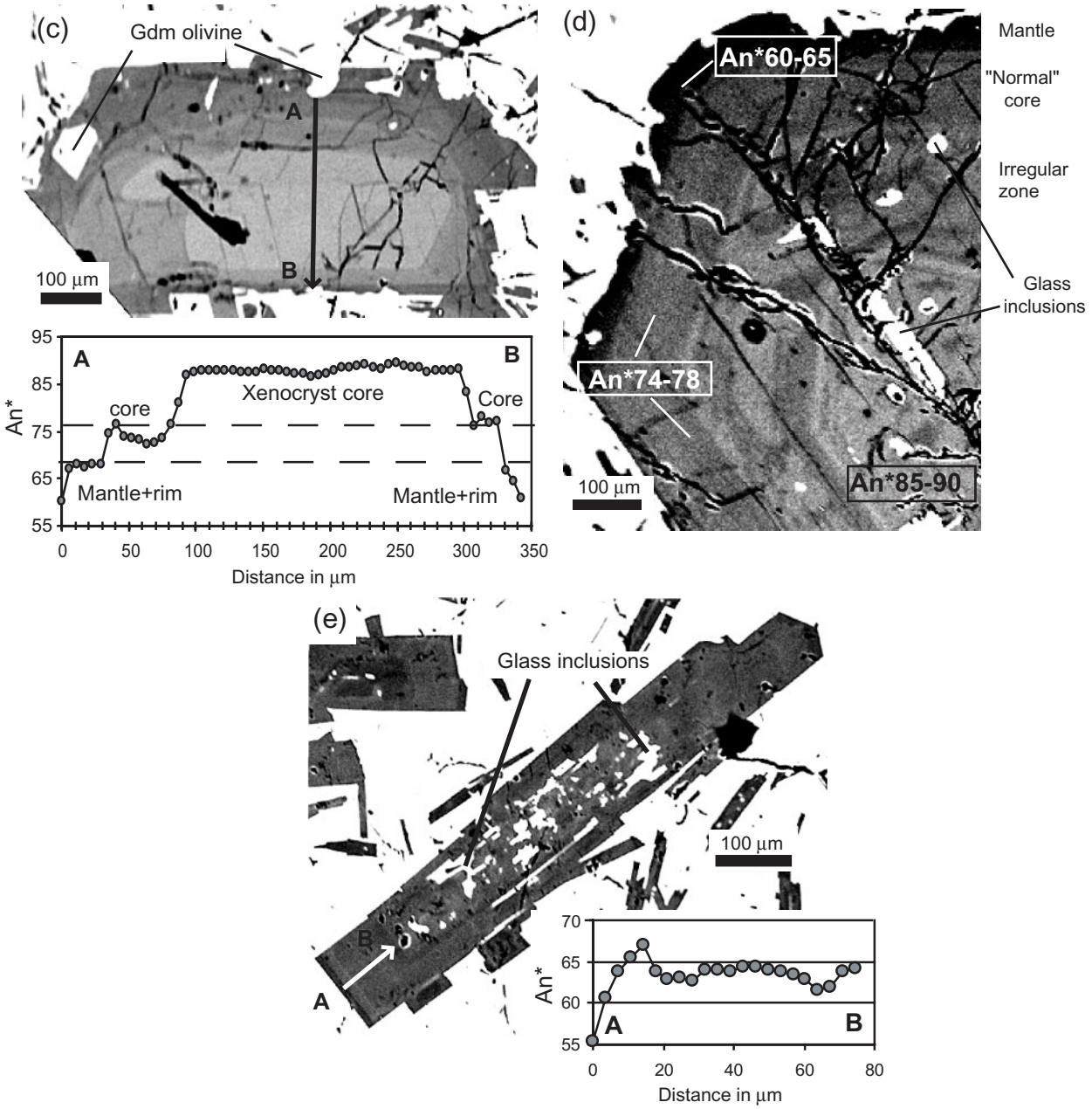

Fig. 7. Continued.

We thus conclude that liquid compositional variations during flow advance were minor and not related to distance from source.

Variations in the glass composition and surface morphologies (degree of crust disruption) of lava quenched along single flows were also investigated. The two sets of samples collected along proximal LF lavas show a marked down-flow increase in glass MgO that matches a change from shelly to spiny surfaces (Fig. 13a). However, this pattern is not apparent in the other sample sets collected. The set of L29- samples collected from a sequence of lobes at medial distances from the fissure, cover a small range in glass composition (4·44–4·51 wt % MgO, Table 9) that does not correlate with down-flow distance. The suite of L63- samples collected along a distal lobe display a general decrease in glass MgO with down-flow distance, but a proximal sample (L63-6) plots distinctly away from this trend, for no obvious reasons (Fig. 13b). Glass composition along that lobe does not correlate with the vesicular

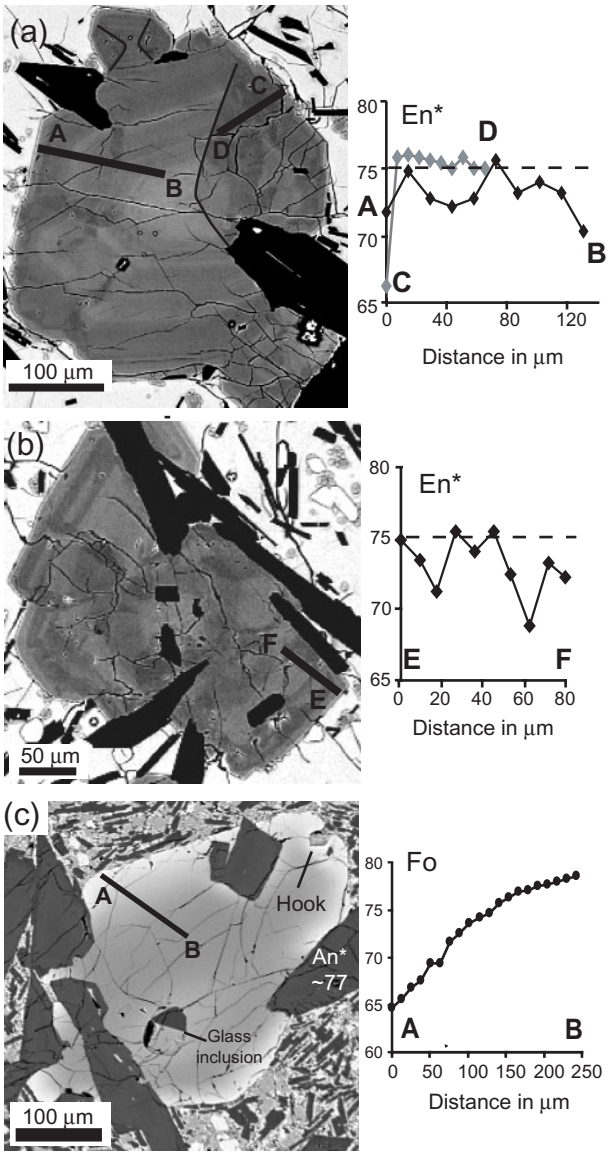

Fig. 8. Internal zoning in clinopyroxene and olivine. (a) and (b) BSE images and microprobe profiles of clusters of groundmass clinopyroxene showing irregular zoning. The sector zoning in (a) should be noted (thin dark lines). Sample L17-1. (c) BSE image and microprobe profile of olivine phenocryst showing progressive normal zoning at rims (note colour zoning). Sample L7-1. The hook-shape of the crystal edge should be noted. The crystal is intergrown with plagioclase phenocryst laths with An-rich cores.

texture of the sample or the type of lava surface sampled (spiny, slabby or rubbly, Fig. 13). Sample L63-9, collected from the rubbly frontal surface of the flow, contains matrix glass that is more heterogeneous and more evolved than that in other samples (compare Fig. 13c with Fig. 10), probably because it was affected by post-emplacement cooling (see below).

FTIR analysis of matrix glass water contents in a selection of samples detected a range of 0·076–0·102 wt % in tephra and 0–0·352 wt % in lava, with a mean of 0·1 wt % (Table 10). We note that three patches analysed in lava sample L18-1 gave significantly higher H_2O contents than the mean (~0·2–0·35 wt %).

Least-squares calculations

The program of Herrmann & Berry (2002) was used to estimate the phase assemblage and amounts of crystallization required to reproduce tephra and lava matrix glass compositions from the whole-rock. The results, compositions used, values of density for volume conversion, and residuals are reported in the Appendix (Tables A1 and A2). The sum of the residuals squared is most often <0·1 and always <0·5, indicating a good fit (Herrmann & Berry, 2002). Results are plotted against glass MgO content in Fig. 14. The calculated amounts of crystallization are 8–11 vol. % to form tephra glasses and 20–33 vol. % to form the range of lava glasses (Fig. 14). Calculated phase proportions for tephra samples are variable (60–70 vol. % plagioclase, 20–35 vol. % clinopyroxene and 5–10 vol. % olivine) and not correlated with glass MgO. In contrast, those calculated for the lava follow a narrow trend with glass MgO and vary in the range 65–70 vol. % plagioclase, 17–30 vol. % clinopyroxene and 10–15 vol. % olivine. The range of glass composition measured in sample L63-9 implies crystallization of 32–42 vol. % of different amounts and relative proportions of plagioclase, olivine and clinopyroxene (Fig. 14). Results compare well with groundmass textural data (Fig. 14), except that clinopyroxene (and hence total crystallinity) is overestimated by about a factor of two. We attribute this difference to an artefact of the method used for textural analysis. In fact, many of the lava selvages analysed by BSE imaging contained patches of finely crystallized glass affected by post-emplacement (quenching) cooling. This glass is similar in colour to clinopyroxene in BSE images, leading to a systematic overestimation of the clinopyroxene phase by textural analysis. This error also accounts for the large standard deviations associated with repeated analyses within individual samples.

Crystal–glass compositional gradients

At the transition between the lava outer selvage containing clear homogeneous glass and the opaque lava interior, there is a zone where plagioclase crystals develop dark fibrous, dendritic overgrowths that, going inwards, gradually spread to occupy all the area between crystals (Fig. 15a). Viewed in high-contrast BSE images, the dendrites form dark grey zones with diffuse edges (Fig. 15b) and there are thin white boundary layers bordering plagioclase faces, especially where the crystal edges are irregular (Fig. 15b). Microprobe profiles across these white boundary layers detected an obvious compositional gradient that is

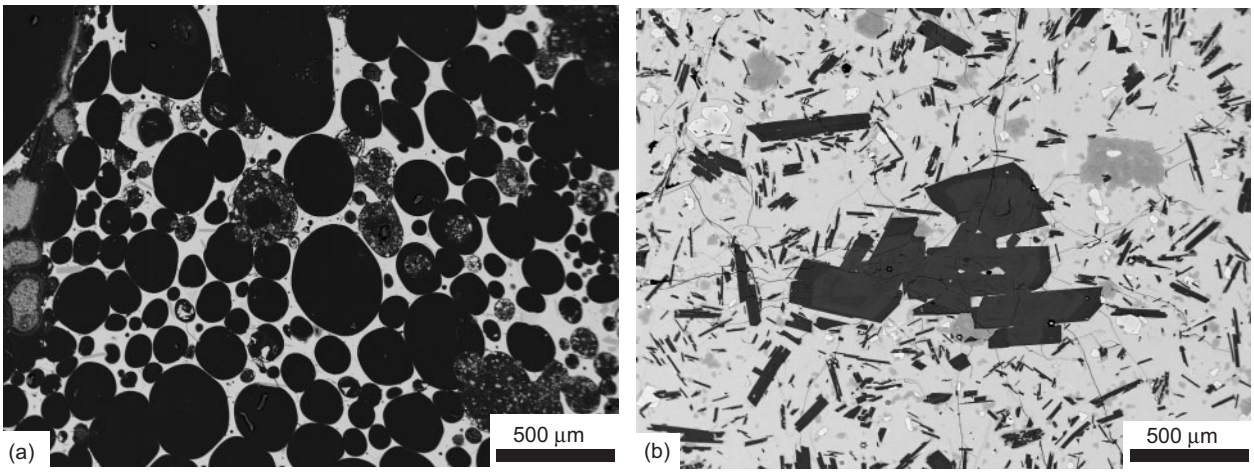

Fig. 9. Representative BSE images of glassy samples of (a) tephra (sample 22-08-83) and (b) lava selvage (sample L17-1). Plagioclase appears dark grey, clinopyroxene light grey and olivine white. It should be noted that Fe oxides are absent in Laki lava selvages.

Table 5: Mineral mode of selected samples (BSE image analysis)

Sample	*N*	Area (mm^2)	Pl%	Cpx%	Ol%	Cr.%
Vent tephra						
16-08-83	5	6·8	1·7	1·4	0·2	3·8
18-08-83	4	8·2	3·8	3·4	<0·1	7·2
22-08-83	4	16·7	4·8	1·4	0·0	6·2
Lava selvages						
L17-1	9	17·1	14 (2)	5 (2)	2 (1)	21 (2)
L18-1	10	16·2	18 (2)	6 (2)	2 (1)	26 (3)
L21-1	4	9·8	19 (1)	10 (2)	5 (1)	34 (2)
L43-2	5	9·5	18 (2)	8 (3)	2 (1)	29 (4)
E3-5	2	4·2	17 (3)	14 (2)	2 (1)	34 (4)
L55-10	10	12·4	18 (2)	10 (2)	2 (1)	29 (7)
L63-5	9	17·5	15 (2)	8 (3)	2 (1)	26 (5)
L63-6	7	15·6	19 (1)	14 (2)	5(2)	38 (3)
L63-7	12	24·3	17 (2)	11 (2)	3 (1)	31 (2)
L63-8	10	21·7	19 (1)	9 (3)	3 (1)	31 (1)
L63-10	8	17·7	22 (2)	10 (2)	4(1)	36 (1)
L63-1	10	16·3	20 (2)	12 (1)	5 (1)	37 (2)

All proportions normalized to 100% on vesicle-free basis. *N*, number of BSE images analysed. Area, total area of glass analysed (vesicle free). Pl, plagioclase; Ol, olivine; Cpx, clinopyroxene; Cr.%, total crystal content (balance of the mode is glass). Average of multiple analyses for each lava sample reported with standard deviation in parentheses. For vent tephra samples, because of the high variation in vesicularity between images, the area covered by each mineral phase in all images analysed was added, divided by the total area studied and normalized to 100%. The vesicularity of BSE images of vent tephra analysed varied in the range of 40–50 vol.% for sample 16-08-83, 38–53 vol.% for sample 18-08-83, and 82–88 vol.% for sample 22-08-83.

Table 6: Proportions of vesicles and crystal types in some lava surface samples

Sample	Number of counts	Vesicularity	Normalized to 0% vesicles		
			Gdm	Pheno	Cr.
L7-1	500	39·0	55·6	2·3	57·9
L7-1	465	31·4	58·6	1·3	59·9
L7-1	1000	32·0	54·1	0·7	54·9
L4-1	482	24·7	58·4	6·3	64·7
L4-2	500	15·4	27·0	7·6	34·5
L13-1	500	27·6	42·3	4·1	46·4

Results from point counts (vol.%). Gdm, groundmass crystals; Pheno, phenocrysts; Cr., total crystallinity (the balance of the mode is glass).

characterized by a relative enrichment of the glass in MgO, FeO, TiO_2, MnO, P_2O_5 and K_2O, and depletion in CaO and Al_2O_3 (e.g. Fig. 15c). In a few cases, similar gradients were observed along olivine and clinopyroxene crystals in the same zone, but were less well developed.

INTERPRETATIONS

Crystallization history of the magma

Crystal textures and compositions indicate that crystallization of the Laki magma took place in two major steps. Phenocryst cores formed first, growing on partially resorbed xenocrysts (step 1). Phenocryst mantles and rims formed at a later stage, accompanied by nucleation and growth of compositionally similar groundmass crystals (step 2). The distinctly lower An content of plagioclases formed at step 2 compared with those formed at

Table 7: Results of manual measurements of crystal numbers on BSE images

Sample	Cr.%	Area (mm^2)	Plagioclase		Olivine	
			N	N_a (mm^{-2})	N	N_a (mm^{-2})
Vent tephra						
16-08-83	6·81	8·60	133	20	1	0·1
18-08-83	8·23	10·60	427	52	9	1·1
Lava selvages						
L17-1	2·04	23·90	918	450	289	142
L66-3	1·84	27·10	356	194	61	33
L18-1	2·75	30·20	435	158	54	20

Cr., total crystallinity calculated using glass composition and least-squares calculations (see Table A1); Area, total area of matrix glass measured (vesicle free); N, number of crystals counted; N_a, number density.

Table 8: Average composition of Laki matrix glasses: vent tephra

Sample	15-08-83	16-08-83	18-08-83	22-08-83
SiO_2	50·58 (0·122)	50·72 (0·045)	50·66 (0·107)	50·49 (0·087)
TiO_2	3·01 (0·032)	2·99 (0·054)	2·97 (0·027)	3·05 (0·036)
Al_2O_3	13·17 (0·038)	13·07 (0·051)	13·10 (0·062)	13·09 (0·105)
FeO	14·11 (0·050)	14·06 (0·094)	14·49 (0·096)	14·25 (0·084)
MnO	0·23 (0·006)	0·23 (0·007)	0·24 (0·012)	0·23 (0·009)
MgO	5·60 (0·061)	5·59 (0·042)	5·43 (0·048)	5·49 (0·037)
CaO	9·65 (0·067)	9·71 (0·066)	9·49 (0·061)	9·83 (0·093)
Na_2O	2·84 (0·043)	2·84 (0·030)	2·82 (0·030)	2·76 (0·042)
K_2O	0·46 (0·014)	0·46 (0·006)	0·46 (0·010)	0·46 (0·011)
P_2O_5	0·35 (0·014)	0·34 (0·013)	0·34 (0·021)	0·35 (0·028)
Total	99·37 (0·192)	99·04 (0·164)	99·10 (0·126)	99·12 (0·224)

Data in wt %, normalized to 100% (except total). Standard deviation in parentheses. Number of analyses averaged for each sample reported in Table 1.

step 1 suggests a major change in the conditions of crystallization. Signs of resorption at some phenocryst core–rim boundaries (Figs 5b and c), a diffuse core–rim transition across some crystals, and formation of irregular zoning with inclusion of glass patches (Fig. 7b) indicate that some disequilibrium occurred prior to and during plagioclase phenocryst growth. The systematic normal zoning of olivines (Fig. 8c) suggests, in contrast, that olivine crystals maintained surface chemical equilibrium with the liquid throughout their growth. In groundmass phases, frequent irregular zoning in clinopyroxene (e.g. Figs 8a and b) implies fluctuations in crystal growth rates and local disequilibrium at the crystal–liquid interface (Downes, 1974; Tsuchiyama, 1985). This also applies to some plagioclase (Fig. 7e). The abundance of melt inclusions (Figs 5d–f) implies that the faces of the crystals developed skeletal and hopper shapes throughout growth (e.g. Faure & Schiano, 2004; Kohut & Nielsen, 2004).

We propose that the phenocrysts formed prior to eruption in a magma chamber with relatively water-rich conditions allowing high-An ($An^*_{70–82}$) plagioclase phenocrysts to grow (step 1). Low melt undercooling favoured planar crystal faces (euhedral morphologies) and crystal synneusis by minimization of surface energies (e.g. Vance, 1969). It also favoured crystal growth over nucleation, forming low numbers of large crystals (e.g. Fig. 5a). Crystal compositions are relatively homogeneous, consistent with equilibrium conditions, whereas dynamical processes in the chamber or along its walls may account for some irregular zoning and inclusions of rounded phenocrysts into aggregates. Crystallization in step 2, involving overgrowth on phenocrysts and groundmass crystallization, is best explained by the effects of degassing of the magma during ascent (e.g. Sparks & Pinkerton, 1978). Degassing of the Laki magma upon eruption was intense and shallow-seated (Thordarson & Self, 1993; Thordarson *et al.*, 1996). The exsolution level can be estimated as 10 MPa (~400 m depth) by using the solubility-pressure macro of Newman & Lowenstern (2002) for pure water, basaltic composition, 1150°C and 1 wt % water. Rapid gas loss and a kinetic delay in crystallization can lead to a sharp rise in melt undercooling, yielding a burst of groundmass crystallization and a drop in An content of newly formed plagioclase (e.g. Hammer & Rutherford, 2002). The high number density and small size of groundmass crystals compared with phenocrysts suggest an increase in crystal nucleation rates, which typifies a rise in degree of melt undercooling (e.g. Couch *et al.*, 2003). The fact that some plagioclase phenocrysts have a diffuse compositional gradient at the core–mantle transition may imply that they continued to grow during degassing, readjusting to the drop in water concentrations in the liquid. Others experienced dissolution, perhaps as a result of disequilibrium with the degassed melt. This effect was observed by Hammer & Rutherford (2002) in dynamic experiments in which the charges experienced large and rapid decompression and thus large effective undercooling. Olivine probably kept growing during degassing, as implied by a continuous re-equilibration to the changing liquid composition. Irregularities in clinopyroxene growth led to complex zoning patterns.

Table 9: Average composition of Laki matrix glasses: lava selvages

Sample:	E3-5	L14-3	L14-6	L14-7	L17-1	L17-3
SiO_2	50·14 (0·262)	50·49 (0·157)	50·63 (0·097)	50·42 (0·057)	50·40 (0·072)	50·43 (0·095)
TiO_2	4·07 (0·035)	3·50 (0·053)	3·57 (0·041)	3·54 (0·042)	3·63 (0·043)	3·61 (0·044)
Al_2O_3	11·49 (0·027)	12·26 (0·107)	11·88 (0·076)	12·41 (0·148)	11·92 (0·040)	11·99 (0·140)
FeO	17·10 (0·541)	15·32 (0·096)	15·50 (0·056)	15·16 (0·126)	15·77 (0·110)	15·65 (0·143)
MnO	0·27 (0·015)	0·25 (0·011)	0·27 (0·012)	0·24 (0·016)	0·25 (0·011)	0·25 (0·009)
MgO	4·29 (0·112)	4·99 (0·094)	4·82 (0·051)	4·90 (0·122)	4·79 (0·052)	4·86 (0·062)
CaO	9·05 (0·142)	9·79 (0·050)	9·57 (0·050)	9·79 (0·124)	9·58 (0·060)	9·53 (0·040)
Na_2O	2·52 (0·097)	2·48 (0·078)	2·85 (0·027)	2·60 (0·100)	2·72 (0·075)	2·75 (0·040)
K_2O	0·59 (0·015)	0·52 (0·015)	0·52 (0·006)	0·52 (0·011)	0·53 (0·020)	0·54 (0·014)
P_2O_5	0·47 (0·009)	0·39 (0·015)	0·39 (0·020)	0·40 (0·030)	0·40 (0·019)	0·39 (0·017)
Total	99·24 (0·164)	98·93 (0·320)	99·18 (0·203)	98·48 (0·341)	99·31 (0·175)	98·96 (0·205)

Sample:	L17-5	L17-6	L18-1	L21-1	L29-13	L29-15
SiO_2	50·40 (0·079)	50·50 (0·080)	50·04 (0·200)	50·40 (0·106)	50·10 (0·099)	50·14 (0·067)
TiO_2	3·51 (0·062)	3·73 (0·019)	4·08 (0·041)	3·85 (0·051)	4·02 (0·048)	3·97 (0·031)
Al_2O_3	12·14 (0·104)	11·99 (0·083)	11·42 (0·131)	11·73 (0·127)	11·53 (0·087)	11·50 (0·026)
FeO	15·61 (0·118)	15·53 (0·094)	16·75 (0·100)	16·22 (0·085)	16·74 (0·136)	16·65 (0·109)
MnO	0·26 (0·007)	0·25 (0·011)	0·27 (0·010)	0·25 (0·016)	0·26 (0·013)	0·27 (0·010)
MgO	5·02 (0·056)	4·80 (0·055)	4·41 (0·070)	4·57 (0·038)	4·44 (0·077)	4·51 (0·033)
CaO	9·55 (0·041)	9·45 (0·042)	9·17 (0·039)	9·42 (0·047)	9·10 (0·092)	9·25 (0·045)
Na_2O	2·61 (0·147)	2·80 (0·038)	2·80 (0·062)	2·57 (0·025)	2·75 (0·077)	2·68 (0·099)
K_2O	0·52 (0·021)	0·53 (0·013)	0·60 (0·008)	0·57 (0·011)	0·60 (0·010)	0·58 (0·016)
P_2O_5	0·38 (0·033)	0·41 (0·021)	0·45 (0·017)	0·42 (0·021)	0·47 (0·025)	0·45 (0·020)
Total	98·68 (0·352)	98·80 (0·211)	99·50 (0·453)	99·05 (0·096)	100·22 (0·187)	99·25 (0·239)

Sample:	L29-18	L33-1	L4-2	L43-2	L55-10	L63-1
SiO_2	50·22 (0·042)	50·23 (0·115)	50·30 (0·249)	50·21 (0·165)	50·13 (0·218)	50·35 (0·116)
TiO_2	3·94 (0·037)	3·86 (0·054)	3·98 (0·185)	3·88 (0·038)	3·85 (0·076)	4·02 (0·056)
Al_2O_3	11·66 (0·053)	11·72 (0·036)	11·46 (0·173)	11·68 (0·042)	11·56 (0·095)	11·58 (0·018)
FeO	16·55 (0·141)	16·26 (0·115)	16·93 (0·211)	16·20 (0·178)	16·48 (0·140)	16·39 (0·130)
MnO	0·26 (0·010)	0·25 (0·012)	0·26 (0·010)	0·27 (0·011)	0·27 (0·008)	0·28 (0·015)
MgO	4·45 (0·022)	4·62 (0·053)	4·41 (0·073)	4·75 (0·108)	4·63 (0·058)	4·50 (0·049)
CaO	9·12 (0·104)	9·31 (0·062)	8·80 (0·161)	9·50 (0·062)	9·25 (0·102)	9·31 (0·021)
Na_2O	2·79 (0·101)	2·75 (0·091)	2·77 (0·068)	2·52 (0·228)	2·82 (0·085)	2·54 (0·090)
K_2O	0·58 (0·019)	0·56 (0·010)	0·62 (0·026)	0·54 (0·024)	0·56 (0·019)	0·57 (0·022)
P_2O_5	0·44 (0·023)	0·44 (0·018)	0·47 (0·020)	0·44 (0·019)	0·43 (0·027)	0·45 (0·019)
Total	99·62 (0·288)	99·13 (0·225)	98·98 (0·266)	98·74 (0·200)	99·39 (0·163)	99·47 (0·134)

Sample:	L63-10	L63-5	L63-6	L63-7	L63-8	L66-3
SiO_2	50·39 (0·201)	50·27 (0·047)	50·29 (0·114)	50·11 (0·036)	50·26 (0·146)	50·17 (0·094)
TiO_2	3·95 (0·083)	3·76 (0·049)	4·02 (0·081)	3·91 (0·049)	3·88 (0·058)	3·84 (0·043)

(continued)

Table 9: Continued

Sample:	L63-10	L63-5	L63-6	L63-7	L63-8	L66-3
Al_2O_3	11·54 (0·071)	11·76 (0·082)	11·50 (0·071)	11·58 (0·045)	11·73 (0·176)	11·82 (0·069)
FeO	16·62 (0·145)	16·20 (0·079)	17·01 (0·110)	16·39 (0·085)	16·47 (0·126)	16·36 (0·038)
MnO	0·27 (0·010)	0·26 (0·014)	0·28 (0·007)	0·27 (0·015)	0·25 (0·019)	0·25 (0·007)
MgO	4·47 (0·047)	4·67 (0·099)	4·49 (0·064)	4·67 (0·049)	4·62 (0·015)	4·64 (0·029)
CaO	9·01 (0·080)	9·48 (0·060)	9·14 (0·040)	9·32 (0·033)	9·29 (0·054)	9·19 (0·051)
Na_2O	2·74 (0·059)	2·63 (0·075)	2·21 (0·177)	2·72 (0·067)	2·50 (0·191)	2·73 (0·025)
K_2O	0·59 (0·014)	0·55 (0·020)	0·60 (0·029)	0·59 (0·031)	0·57 (0·014)	0·56 (0·017)
P_2O_5	0·43 (0·021)	0·44 (0·019)	0·46 (0·005)	0·45 (0·021)	0·43 (0·019)	0·43 (0·026)
Total	99·15 (0·344)	99·55 (0·248)	99·27 (0·248)	99·23 (0·181)	99·06 (0·266)	98·78 (0·136)

Location of samples and number of glass analyses averaged reported in Table 1. Standard deviation in parentheses. Analyses normalized to 100%, total reported is original.

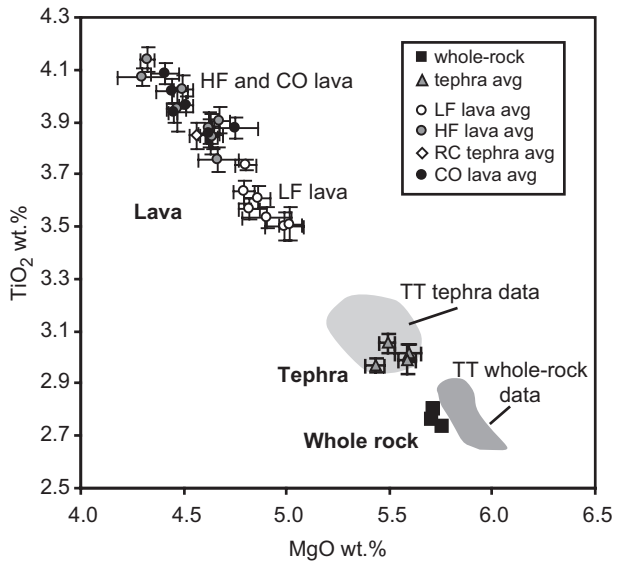

Fig. 10. Plot of whole-rock (XRF) and tephra and lava matrix glass (EMPA) data as a function of TiO_2 wt % vs MgO wt %. Average matrix glass compositions are plotted for each sample along with error bars showing the standard deviation of multiple analyses (data in Table 7). Errors associated with the analytical method, estimated from standard glass data, are ±0·095 MgO wt % and ±0·045 TiO_2 wt % (see Table 2). Dark grey fields represent extent of whole-rock (ICP-MS) and tephra matrix glass (EMPA) data of Thordarson *et al.* (1996) and T. Thordarson (unpublished).

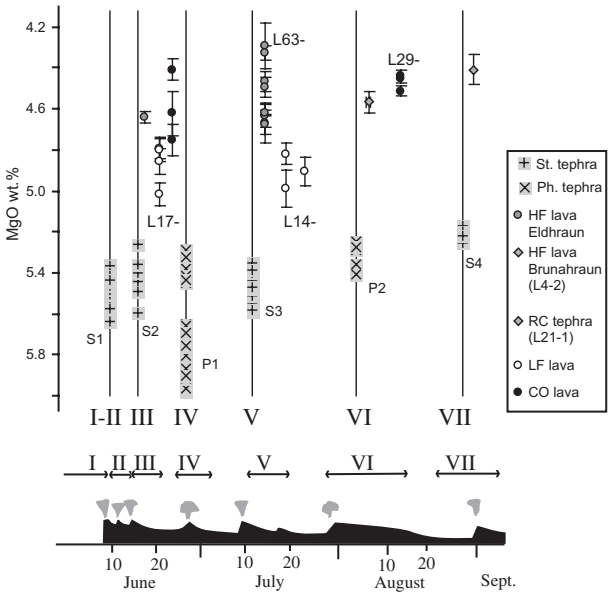

Fig. 11. Plot of average glass MgO with standard deviation vs estimated time during the eruption. Sketch at bottom showing variations in lava production rates as a function of time is adapted from Thordarson *et al.* (1996). Roman numerals indicate eruptive episodes. Crosses with grey squares represent tephra data from this study, Thordarson *et al.* (1996) and T. Thordarson (unpublished data). S1–S4 and P1, P2, are tephra units defined by Thordarson & Self (1993). Tephra: St., strombolian; Ph., phreatomagmatic; RC, rootless cone. Position of lava from high fountaining (HF), low fountaining (LF) and cone-building (CO) phases in timing is arbitrary. Data for samples collected along single flows are labelled by starting sample number (L14-, L17-, L29- and L63-). Further information about the inferred timing of quenching of samples is given in the text.

Estimated crystallization conditions

Models of mineral-equilibria were used to constrain the conditions of crystallization of phenocryst cores and groundmass crystals. Temperatures were estimated using the olivine–glass (liquid) thermometer of Beattie (1993). Then, to assess water content concentrations, these temperatures were compared with those calculated using the hydrous, plagioclase–glass (liquid) model of Putirka (2005) for various values of H_2O content. It was assumed that the phenocryst cores were in chemical equilibrium with the whole-rock composition at magma chamber conditions, and that the groundmass crystals

were in equilibrium with matrix glasses at surface conditions. We use a quartz–fayalite–magnetite (QFM) buffer, on the basis of calculations using the model of Sugawara (2000), plagioclase–olivine pairs and conditions of 0·1 MPa and 1140°C. For magma chamber conditions, a pressure of 250 MPa was used, consistent with storage of the magma at 10 km depth, at the base of the local Icelandic crust (Sigmarsson *et al.*, 1991). Using the representative crystal compositions, all the whole-rock compositions and the average tephra and lava glass compositions collected in this study yield the results reported in Table 11.

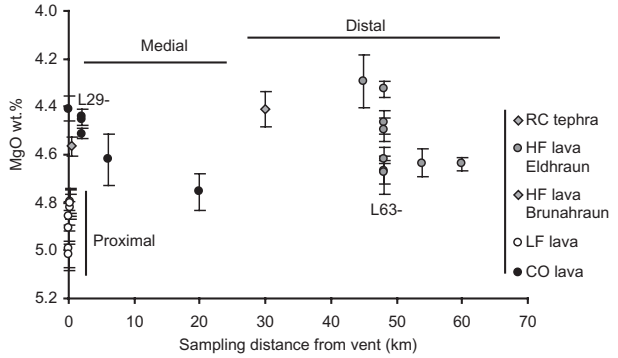

Fig. 12. Plot of average glass MgO in lava samples vs distance from the vent. The absence of correlation and range of variations measured in samples collected along single flows should be noted (e.g. samples starting with numbers L63- and L29-).

The Beattie (1993) model gives 1157–1159 ± 10°C as the temperature of phenocryst core formation, 1144–1149 ± 10°C for groundmass crystal formation in tephra, and 1116–1133 ± 10°C for groundmass crystal formation in lava. Temperature estimates using the Putirka (2005) model agree with those from the Beattie (1993) model if 1 wt % H_2O is assumed for the conditions of phenocryst core formation and 0–0·1 wt % H_2O for groundmass crystal formation (Table 11). This is in accord with the above interpretations and water contents measured by FTIR in matrix glasses. Small discrepancies can be attributed to the limits of both models and crystal–liquid disequilibrium at high undercooling.

An independent estimate of the Laki magma's pre-eruptive water content can be made using melt inclusion data from Métrich *et al.* (1991). They measured a water content of 0·47 wt % in olivine-tholeiite glass inclusions hosted in olivine xenocrysts. Assuming that the composition of those inclusions reflects the parental magma to the Laki magma (e.g. Bindeman *et al.*, 2006), and applying a fractionation model (Boudreau, 1999), implies a concentration of ~1 wt % H_2O in the Laki magma. However, this value may have been lower by up

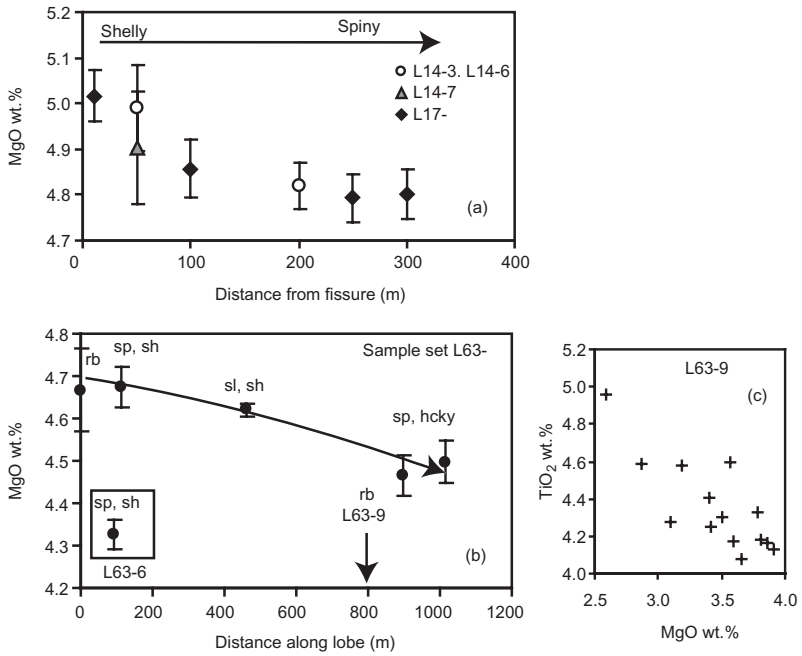

Fig. 13. Variation of glass MgO wt % in samples collected along single flows. (a) Down-flow decrease in average glass MgO of samples collected along proximal flows emitted during low fountaining activity (L17- denotes all samples starting with number L17-). (b) Variations along a lava lobe on the coastal plain that shows increasing surface brecciation along its length (see Fig. 4). Glass data are plotted as averages with associated standard deviation. Distinctly evolved composition of sample L63-6 is highlighted with square outline. The horizontal axis represents the respective distance of the samples relative to sample L63-5, the most up-flow sample. (c) Multiple analyses of sample L63-9 plotted as TiO_2 vs MgO. Lava surface types: rb, rubbly; sp, spiny; sl, slabby; sh, sheet; hcky, hummocky.

Table 10: Results from FTIR analysis of tephra and lava matrix glasses

Sample	Analysis number	Absorbance (*a*)	Thickness (μm)	H_2O (wt %)
Vent tephra				
16-08-83	1	0·066	72	0·096
18-08-83	1	0·062	85	0·076
18-08-83	2	0·050	85	0·061
18-08-83	3	0·084	85	0·102
18-08-83	4	0·073	93	0·082
Lava				
L14-6	1	0·113	130	0·090
L14-6	2	0·101	130	0·081
L14-6	3	0·142	130	0·114
L17-3	1	0·080	67	0·123
L17-3	2	0·080	67	0·123
L17-3	3	0·010	29	0·036
L18-1	1	0·051	65	0·081
L18-1	2	0·042	65	0·067
L18-1	3	0·137	65	*0·219*
L18-1	4	0·126	182	0·072
L18-1	5	0·101	171	0·061
L18-1	6	0·101	30	*0·352*
L18-1	7	0·088	30	*0·307*
L43-2	1	0·000	22	0·000

H_2O calculated using Beer–Lambert equation (see equation in text), neglecting H_2O_{mol}. Analysis number refers to the analysis of separate locations on the thin-sections. The high water content detected by some analyses in sample L18-1 (values in italics) should be noted.

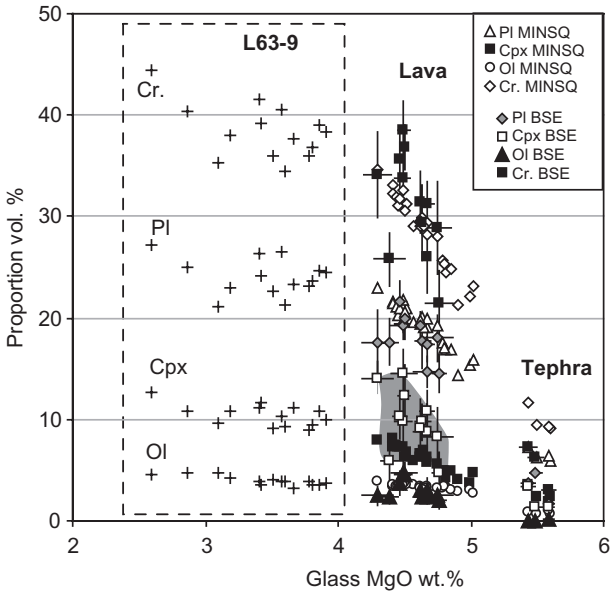

Fig. 14. Results from mass-balance calculations (MINSQ in key) and comparison with groundmass crystal quantification by textural analysis of BSE images (BSE in key). Mineral phase proportions in vol.%. Pl, plagioclase; Ol, olivine; Cpx, clinopyroxene; Cr., total crystallinity. +, Calculations for multiple glass analyses of sample L63-9. Results from textural analysis are recalculated on vesicle-free basis. Vertical error bars show standard deviation of results from textural analysis of separate images of individual samples. Horizontal error bars indicate standard deviation of repeated glass analyses by EMPA. Grey area traces difference between results from BSE and MINSQ methods for clinopyroxene proportions (see text for explanation).

to 20% if, as Sigmarsson *et al.* (1991) have argued, the Laki magma evolved during assimilation of 20% of crustal material.

Controls of eruptive processes on groundmass crystallization

The study of spatio-temporal variations in glass compositions of tephra and lava products, and their correlation with groundmass crystallization, reveals the following pattern. The early explosive phase following fissure opening produced crystal-poor, vesicle-rich tephra. Products from later effusive phases were markedly more crystal-rich and vesicle-poor. Lavas produced by high fountaining and cone-building phases were slightly more crystal-rich and vesicle-poor than lavas emitted during transitional low fountaining activity. Crystallization during lava emplacement was limited and not correlated with the distance and duration of transport of the fluid lava prior to quenching.

This pattern shows that the intensity of groundmass crystallization in the surface products was governed by eruptive dynamics at the vent. We propose that the determining factors were the timing of magma ascent and surface quenching, in turn controlled by magma discharge rates and gas segregation dynamics (e.g. Sparks, 2003). These factors determine the residence time of the melt at sub-liquidus temperature, and thus the time available for degassing and crystallization to proceed. During early explosive phases, rapid magma discharge rates, rapid gas expansion, inefficient gas–melt separation and subsequent shallow fragmentation yielded short crystallization times accounting for crystal-poor products. The observed variety of crystal modes and vesicle and crystal contents in clasts produced during single explosive events may reflect disequilibrium crystal growth. They may also record horizontal and vertical variations in the amount of degassing, cooling and crystallization undergone by separate magma batches prior to quenching.

Lava textures (high groundmass crystallinity, low vesicle content) imply longer degassing and crystallization timescales, allowed by slower magma ascent rates, efficient

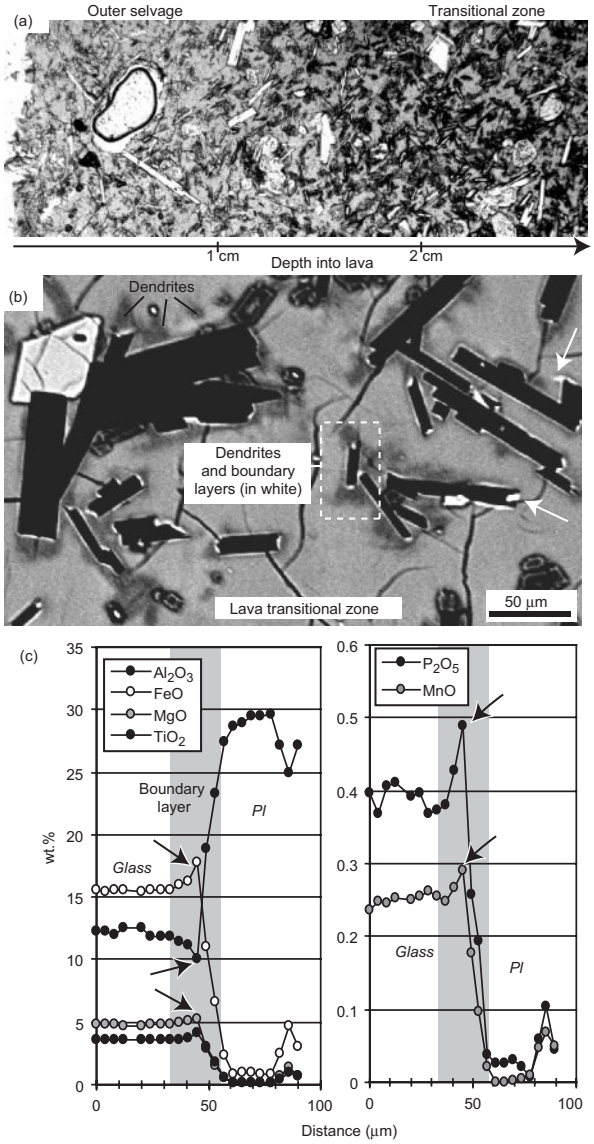

Fig. 15. Boundary layers at plagioclase–glass interface in lava transitional zone. (a) Photograph of representative thin-section across lava sample L17-3 showing gradation from outer selvage with clear light brown interstitial glass to transitional zone with distinct dark layers around plagioclase laths and dark brown interstitial glass. (b) High-contrast BSE image of lava transitional zone showing compositional gradients at plagioclase boundaries (white haloes) and dendritic outgrowth (dark grey patches) (sample L17-3). White arrows point to thick boundary layers. (c) Representative plagioclase (Pl)–glass EMPA traverse across thick boundary layer (sample L14-6, spacing of ~4 μm). Elements showing clear compositional gradients are plotted. Black arrows point to peaks in glass enrichment in elements that are strongly incompatible in plagioclase. The light grey area delimits the inferred thickness of the boundary layer.

Table 11: Parameters and results used in calculation of crystallization conditions based on mineral–melt equilibria

Liquid	Mineral	*T* (°C)	H_2O (wt %)	*P* (MPa)
Pl–liquid equilibria (Putirka, 2005, model A, Table 2, T ± 23°C)				
Whole-rock	An^*_{76}	1185–1189	(0)	(0·1)
Whole-rock	–	1198–1200	(0)	(250)
Whole-rock	–	1153–1155	(1)	(250)
Tephra glasses	An^*_{61}	1146–1148	(0)	(0·1)
Tephra glasses	–	1142–1144	(0·1)	–
Lava glasses	$An^*_{57·5}$	1113–1134	(0)	(0·1)
Lava glasses	$An^*_{57·5}$	1109–1129	(0·1)	–
Ol–liquid equilibria (Beattie, 1993, QFM, T ± 10°C)[1]				
Whole-rock	Fo_{75}	1158–1159		(250)
Tephra glasses	Fo_{72}	1144–1149		(0·1)
Lava glasses	Fo_{66}	1116–1134		(0·1)

Parameters used as inputs in the calculations are in parentheses. Pl, plagioclase; Ol, olivine; *T*, temperature; *P*, pressure.
[1] $K_{Fe/Mg(oliv\text{-}melt)}$ ~0·28 [calculated as molar $(Fe/Mg)_{Olivine}/(Fe/Mg)_{Liquid}$, using total FeO], which is typical of equilibrium conditions (e.g. Sisson & Grove, 1993).

gas separation from the rising magma, and magma effusion at the surface. The relatively higher number density of crystals in the lava compared with tephra (Table 7) suggests that crystal nucleation was facilitated. This may partly result from magma and lava shearing during ascent along the conduit walls and fountaining at the vent. This increases volumetric diffusion (Kouchi *et al.*, 1986) and creates nucleation sites by mechanical breakage of early formed crystals. Lava emitted by low fountaining shows a coupled down-flow increase in crystallinity and decrease in vesicularity that may reflect a late re-equilibration of the melt to the decompression effects. The comparatively higher crystallinity and lower vesicularity of lava produced during other eruptive phases can be accounted for by (1) added lava stirring and heat and gas loss in high lava fountains, and (2) decreasing rates of magma ascent and lava production during cone-building phases. Sample L18-1 shows high crystal contents ascribed to cooling of the lava during ponding in a cone prior to effusion. The narrow trend followed by lava glass compositions and crystal modes (Fig. 14) and the small degrees of cooling calculated suggest that chemical equilibrium was achieved in the flowing lava, and that it crystallized along the plagioclase + olivine + clinopyroxene cotectic following degassing-induced crystallization.

The striking petrological similarity of lava quenched at proximal, medial and distal distances from the fissure during single eruptive phases highlights the thermal efficiency of fluid lava transport within flows. Minor variations may result from heat loss by temporary exposure of the lava to the air or extended

storage within flows. The emplacement (liquid) temperatures calculated using the olivine–glass calibration of Beattie (1993) are plotted against distance from the vent in figure 16. Variations away from the near-vent area are within the uncertainty of the calibration (±10°C). Thus, for a maximum transport distance of 60 km, we can consider a maximum cooling of 20°C, giving a maximum down-flow cooling of 0·3°C/km. It is noted that the heat released by crystallization could have buffered the lava temperature upon emplacement, given that 1% of crystallization can raise the melt temperature by ~2°C (Couch *et al.*, 2003; Blundy *et al.*, 2006).

Solidification processes

Finally, some of the data for samples below the upper lava selvage can be related to cooling and crystallization processes that occur after flow emplacement; that is, as the lava is static and solidifies below the outermost quenched part. The high cooling rates in this zone create conditions of diffusion-limited crystal growth, which forms boundary layers along plagioclases and causes dendritic overgrowth because of constitutional undercooling (e.g. Lofgren, 1974; Schiffman & Lofgren, 1982). Slow diffusion causes the elements rejected by plagioclase to accumulate along the interface, and the liquid at the interface becomes depleted in elements that enter plagioclase, creating the compositional gradient (Fig. 15c). Dendrites grow out of these zones and thus are enriched in Fe and Mg relative to the plagioclase, as shown by a dark grey tone in BSE images (Fig. 15b). These textural features have been reproduced in basaltic melts cooled at 80–450°C/h (Schiffman & Lofgren, 1982), which is comparable with the cooling rates measured inside Hawaiian pāhoehoe lobes [600°C/h at 2 cm depth, after Keszthelyi & Denlinger (1996, Fig. 5)], implying that they developed during post-emplacement cooling. In addition, the heterogeneous evolved compositions measured in the matrix glass of sample L63-9 (Fig. 13c) are consistent with post-emplacement crystallization penetrating below the transitional zone. Least-squares calculations estimate the amounts of crystallization involved to have been 32–42 vol. % (Fig. 14, Table A1). The large variation in the proportions of mineral extracted, in particular for plagioclase, probably represents disequilibrium crystallization (see Hammer & Rutherford, 2002). The temperature range estimated (1070–1110°C, Fig. 16) is also consistent with post-emplacement cooling prior to complete solidification. The local high water contents measured by FTIR in sample L18-1 (Table 8) may also be a post-emplacement effect caused by the enrichment of the liquid in volatiles during differentiation. Concentrating 0·2–0·3 wt % H_2O in the melt (from an initial 0·1 wt % H_2O) would, however, require up to 80 wt % of crystal fractionation and severally deplete the liquid in MgO (~0·4–1·9 wt % MgO), according to the PELE model. It is thus unclear if those measurements are real or analytical errors. These data altogether stress the necessity of analysing clear, homogeneous matrix glasses from the uppermost glass selvage to infer the state of the lava when it was fluid. They also highlight the sharp gradient in temperature (and cooling rates) that exists across lava margins, which demonstrates the

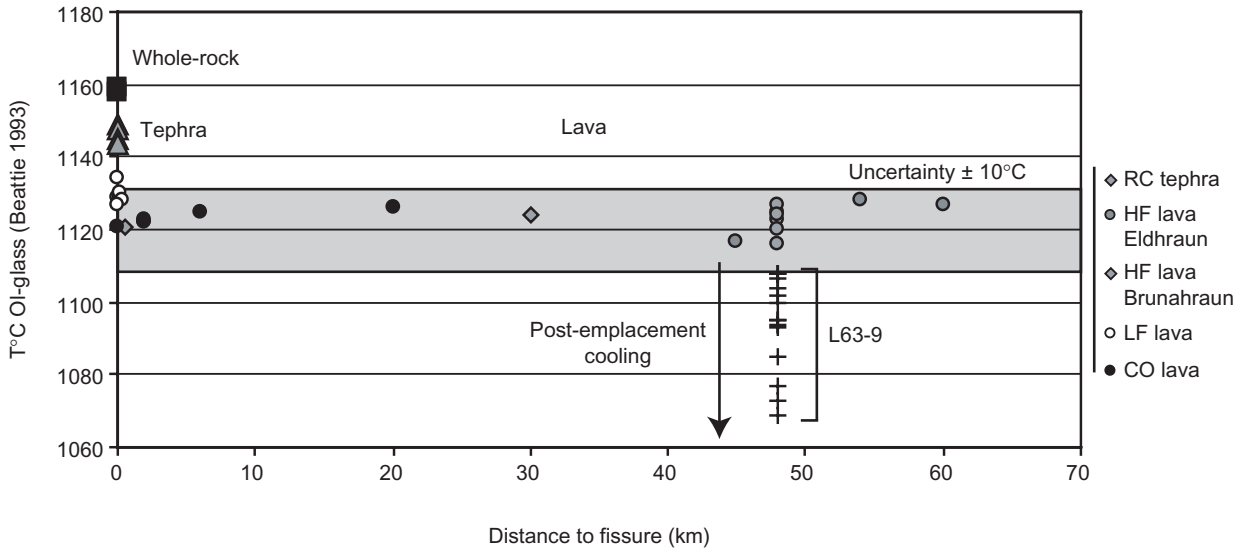

Fig. 16. Calculated temperature of lava emplacement vs distance from the fissure. Values obtained applying olivine–glass thermometer of Beattie (1993) to whole-rock and matrix glass composition data from this study. Matrix glass composition used is average normalized to 100%. Grey rectangle shows extent of model uncertainty (±10°C). Symbols in key are explained in the caption of Fig. 11. Grey triangles, tephra samples; black squares, whole-rock samples. +, Results for multiple analyses of sample L63-9.

degree of thermal insulation provided by the outer millimetre-thick lava skin.

Model of the evolution of the magma–lava during the Laki eruption

The above results constrain a general model for the evolution of the Laki magma and fluid lava during the eruption. The main steps in magma and lava evolution through crystallization are sketched in Fig. 17 (A, magma storage; B, shallow degassing; C, tephra quenching; D, lava fountaining or storage in cone; E, lava flow emplacement). Phenocryst cores grew prior to eruption in an ~10 km deep magma chamber equilibrated at 250 MPa, 1150–1160°C and with ~1 wt % dissolved H_2O (A in Fig. 17). During the eruption, the magma ascended, decompressed, degassed, and became undercooled as a result of a rise in liquidus temperature (B in Fig. 17). This resulted in phenocryst overgrowth and groundmass crystallization. At atmospheric pressure, experiments indicate that plagioclase forms at 1170–1180°C in the anhydrous Laki magma, olivine at 1150–1160°C and clinopyroxene at ~1150°C (Bell & Humphries, 1972). Eruption temperatures of ~1140°C thus imply undercooling of ~10–40°C, consistent with formation of large numbers of skeletal crystals (e.g. Kouchi *et al.*, 1986). During the early explosive phase, the time between degassing and quenching was too short for crystallization to proceed to the extent at which the melt was re-equilibrated, so heterogeneous, crystal-poor tephra was erupted (C in Fig. 17). As the eruption progressed, the magma ascended at lower rates and extensively degassed at shallow levels, in lava fountains or within storage in late-formed cones (D in Fig. 17). Intense crystallization resulted, re-equilibrating the melt and producing lava with a high apparent viscosity

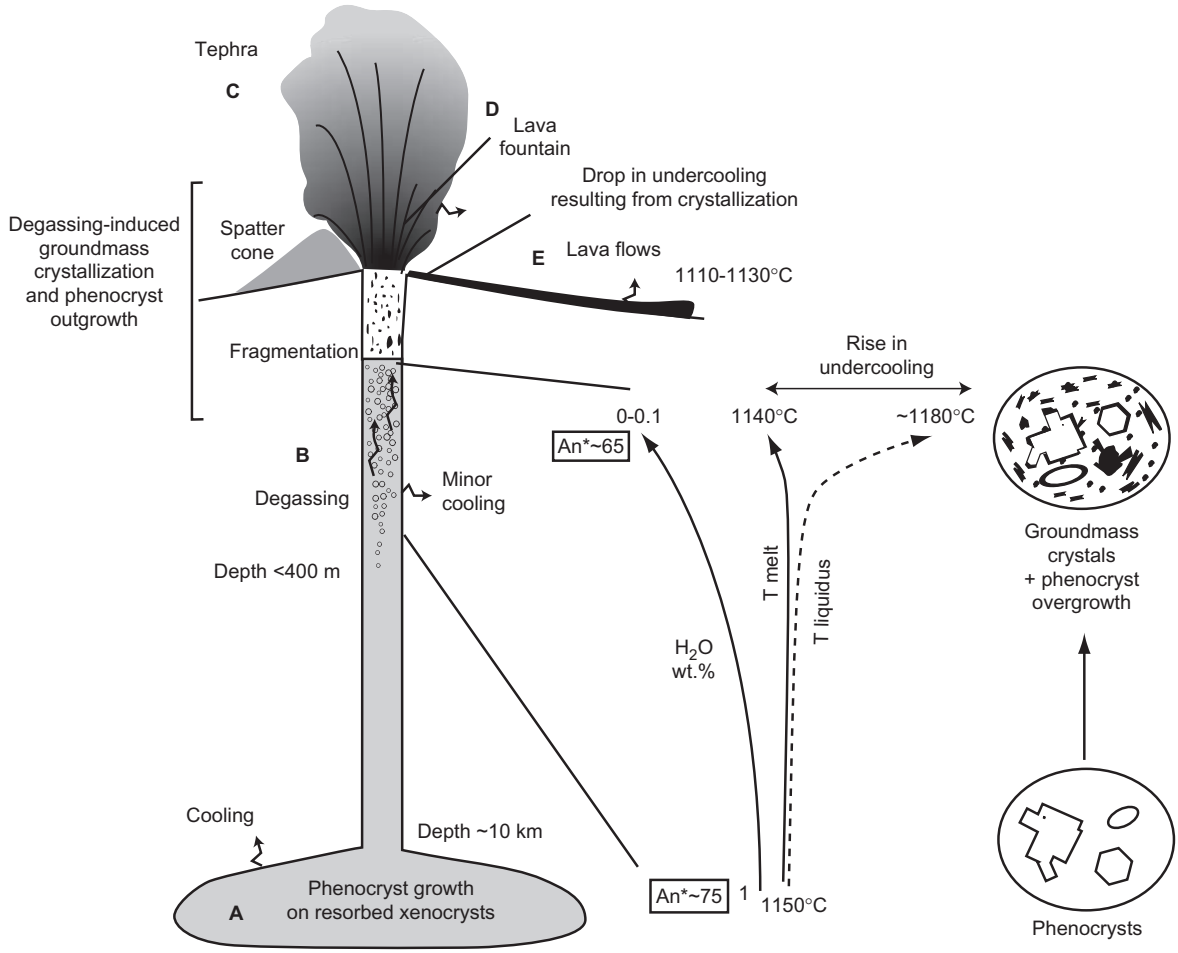

Fig. 17. Schematic representation of the evolution of magma and lava during the Laki eruption. *T*, temperature. A, magma storage; B, shallow degassing; C, tephra quenching; D, lava fountaining or storage in cone; E, lava flow emplacement. Sketch on lower right indicates the simultaneous evolution of melt H_2O content, equilibrium plagioclase composition (An*), melt liquidus temperature, and degree of melt undercooling in shallow rising magma, which leads to groundmass crystallization and phenocryst overgrowth. Sketch of textural evolution in ellipses (white-filled symbols, phenocryst cores; dark-filled symbols, compositionally similar groundmass crystals and phenocryst overgrowths).

(see below). Transport of the fluid lava to the active flow front was nearly isothermal, probably balanced by the heat released by minor amounts of cooling-induced crystallization (E in Fig. 17). Finally, the fluid lava core rapidly cooled and fully crystallized below the outer, insulating skin formed upon air contact.

Groundmass crystallization and lava rheology

Calculations were made to estimate the impact of degassing, cooling and crystallization on the viscosity of the Laki magma upon eruption. The model of Giordano & Dingwell (2003*a*) was used to compute liquid viscosities at the temperatures calculated using Beattie (1993) (plotted in Fig. 16). We then applied the Einstein–Roscoe equation (Pinkerton & Stevenson, 1992) to include the effects of crystal concentration, using crystal contents calculated with the least-squares method and a value of 0·6 for particle concentration at solid state (Marsh, 1981). In figure 18 results are plotted against distance from the vent. The viscosity of the Laki magma at depth is estimated at 1110–1140 Pa s (whole-rock composition, 3 vol. % crystals), that of the magma erupted as tephra at 1600–2100 Pa s, and that of the magma emplaced as lava as 5400–24 000 Pa s (Fig. 18). These are maximum estimates, as the role of water is not included and this lowers the viscosity. For example, for Etna alkali basalt, the difference between zero and 0·5 wt % water content is an order of magnitude drop in liquid viscosity (Giordano & Dingwell, 2003b, Fig. 7). Using the model of Hui & Zhang (2007) that includes the effects from liquid composition and water, gives similar results to those above (viscosities of 2690, 1250, 758, 258 and 77·5 Pa s for Laki average whole-rock composition, 1150°C and water contents of 0, 0·1, 0·2, 0·5 and 1 wt %).

Crystals can also induce non-Newtonian behaviour, such as a yield strength, by forming a resisting framework, and this effect is particularly important for lath-like crystals such as plagioclase (Pinkerton & Stevenson, 1992; Philpotts & Carroll, 1996; Hoover *et al.*, 2001; Ishibashi & Sato, 2007). We propose that the >20 vol. % of groundmass crystals present in the lava emitted throughout the Laki eruption promoted the formation of rubbly pāhoehoe surface morphologies along the flows.

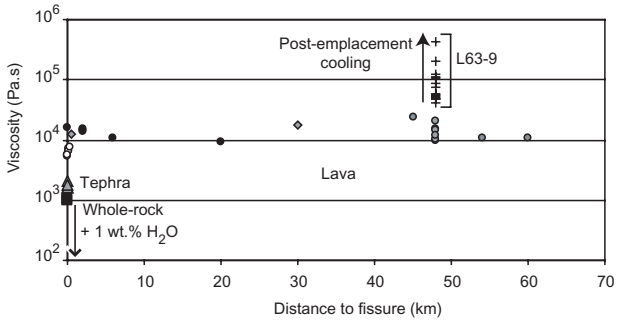

Fig. 18. Calculated bulk viscosity of Laki magma, tephra and lava assuming 0 wt % water and neglecting vesicles. The effect of water in lowering the viscosity is indicated by the arrow and discussed in the text. Symbols as in Fig. 16.

The effect of yield strength is to impede plastic deformation of the lava, slow flow rates, and induce velocity gradients and formation of shear zones at field (Hulme, 1974) and microscopic (Soule & Cashman, 2005) scales. Textural studies suggest that it is a factor that may be more important than shear rates for causing pāhoehoe to ′a′ā transitions (Cashman *et al.*, 1999; Soule *et al.*, 2004; Soule & Cashman, 2005). In fact, emplacement temperatures of 1140°C and bulk viscosities of ~2200 Pa s [estimated by Keszthelyi *et al.* (2004) using typical Laki glass composition, 20 vol. % crystals and 25 vol. % vesicles] bring the Laki lava into the rheological field in which Hawaiian lava develops pāhoehoe or ′a′ā morphologies depending on the shear rates (Hon *et al.*, 2003). The available data show that at the crystal contents of Laki lavas (20–30 vol. %), many Hawaiian pāhoehoe lavas transform to ′a′ā (Lipman *et al.*, 1985; Cashman *et al.*, 1999; Polacci *et al.*, 1999; Soule *et al.*, 2004). We propose that the Laki lava flows were emplaced at shear rates low enough to stay in the transition field between pāhoehoe and ′a′ā (Peterson & Tilling, 1980). This can be linked to the low emplacement slopes of the main body of lava, which promoted the formation of kilometre-scale sheet lobes with a near-stationary, stable crust (Guilbaud *et al.*, 2005). Sustained lava supply from the vent kept the temperature high and the viscosity low in the lobes, which may also have been aided by heat released by syn-emplacement crystallization. Calculated transport cooling rates (<0·3°C/km) are slightly lower than values measured for tube-fed lavas in Hawaii (0·6°C/km, Helz *et al.*, 2003; 0·9°C/km, Thornber, 2001) and much lower than that of channelized lavas (6–7°C/km, Cashman *et al.*, 1999).

The high thermal efficiency of fluid lava transport within the rubbly flows is surprising, given that crust disruption is generally considered as a cooling-enhancing and thus a crystallization-enhancing factor (e.g. Cashman *et al.*, 1999; Harris *et al.*, 2005). This may be compared with the low core cooling rates inferred along dacitic flows with thick, near-stationary blocky cover (Harris *et al.*, 2004). It is reasonable to think that, owing to low shear rates, the rubbly cover formed on the Laki lava added to the thermal insulation provided by the crust alone, reducing any radiative heat loss (see also Keszthelyi *et al.*, 2004, 2006).

CONCLUSIONS

An increasing number of studies have noted the large rheological impact of crystallization triggered by

syn-eruptive ascent degassing (e.g. Sparks & Pinkerton, 1978; Lipman *et al.*, 1985; Hammer *et al.*, 2000; Sparks *et al.*, 2000; Melnik & Sparks, 2002). This study highlights its control on flow emplacement style during a major basaltic eruption. The Laki eruption was characterized by 10 eruptive episodes. During each episode, the magma ascended, decompressed and degassed, first erupting explosively and then mainly effusively. The bulk of the crystals in the products was formed at 10–40°C melt undercooling, which was generated by rapid and shallow exsolution of ~1 wt % H_2O. Explosive products are crystal poor as a result of high magma ascent rates, inefficient degassing and sluggish crystallization. Lavas contain abundant amounts of groundmass crystals because of complete re-equilibration of the melt to the undercooling upon slower ascent and open degassing. Groundmass crystals increased the lava viscosity and yield strength, causing the flows to develop a thick rubbly layer upon emplacement. Our data suggest that, after emission at the vent, the fluid lava was transported to the flow fronts with minor cooling and associated crystallization. This may be due to a balance with latent heat release. Degassing thus had a predominant impact on lava rheology during the Laki eruption. Lava groundmass textures reflect the kinetics of magma ascent and lava extrusion at the vent. We estimate that rubbly surface flows can be as thermally efficient as current tube-fed lavas on Hawaii.

ACKNOWLEDGEMENTS

Dr Andrew Tindle is thanked for his assistance for the microprobe work, Dr Sarah Sephton for her work on the FTIR, Kay Green and Michelle Higgins for thin-section making and polishing, John Watson for the use of the XRF system, and Safak Altunkaynak for assistance in field-work. M. Humphreys, J. Hammer and N. Metrich are thanked for their thorough reviews of the manuscript. This work was supported by the Research Development Fund of The Open University, UK, and the Instituto de Geofisica, Universidad Nacional Autonoma de México.

SUPPLEMENTARY DATA

Supplementary data for this paper are available at *Journal of Petrology* online.

REFERENCES

Beattie, P. (1993). Olivine–melt and orthopyroxene–melt equilibria. *Contributions to Mineralogy and Petrology* **115**, 103–111.

Bell, J. D. & Humphries, D. J. (1972). Lakagigar fissure eruption. Progress in experimental petrology. *National Environmental Council UK Publication Series* **D2**, 110–112.

Bindeman, I. N., Sigmarsson, O. & Eiler, J. (2006). Time constraints on the origin of large volume basalts derived from O-isotope and trace element mineral zoning and U-series disequilibria in the Laki and Grímsvötn volcanic systems. *Earth and Planetary Science Letters* **245**, 245–259.

Blundy, J., Cashman, K. & Humphreys, M. (2006). Magma heating by decompression-driven crystallization beneath andesite volcanoes. *Nature* **443**, 76–80.

Boudreau, A. E. (1999). PELE; a version of the MELTS software program for the PC platform. *Computers & Geosciences* **25**, 201–203.

Cashman, K. V., Thornber, C. & Kauahikaua, J. P. (1999). Cooling and crystallization of lava in open channels, and the transition of pahoehoe lava to a'a. *Bulletin of Volcanology* **61**, 306–323.

Couch, S., Sparks, R. S. J. & Carroll, M. R. (2003). The kinetics of degassing-induced crystallization at Soufrière Hills volcano, Montserrat. *Journal of Petrology* **44**, 1477–1502.

Crisp, J. & Baloga, S. (1990). A model for lava flows with two thermal components. *Journal of Geophysical Research* **95**, 1255–1270.

Dixon, J. E., Stolper, E. M. & Delaney, J. R. (1988). Infrared spectroscopic measurements of CO_2 and H_2O in Juan de Fuca Ridge basaltic glasses. *Earth and Planetary Science Letters* **90**, 87–104.

Dixon, J. E., Stolper, E. M. & Holloway, J. R. (1995). An experimental study of water and carbon dioxide solubilities in mid-ocean ridge basaltic liquids; Part I, Calibration and solubility models. *Journal of Petrology* **36**, 1607–1631.

Downes, M. J. (1974). Sector and oscillatory zoning in calcic augites from M. Etna, Sicily. *Contributions to Mineralogy and Petrology* **47**, 187–196.

Faure, F. & Schiano, P. (2004). Crystal morphologies in pillow basalts; implications for mid-ocean ridge processes. *Earth and Planetary Science Letters* **220**, 331–344.

Giordano, D. & Dingwell, D. B. (2003*a*). Non-Arrhenian multicomponent melt viscosity: a model. *Earth and Planetary Science Letters* **208**, 337–349.

Giordano, D. & Dingwell, D. B. (2003*b*). Viscosity of hydrous Etna basalt: implications for Plinian-style basaltic eruptions. *Bulletin of Volcanology* **65**, 8–14.

Grönvold, K. (1984). The petrochemistry of the Laki lava flow. In: Einarsson, T., Gudbergsson, G. M., Gunnlaugsson, G. A., Rafnsson, S. & Thorarinsson, S. (eds) *Skaftáreldar 1783–1784. Ritgerdir og Heimildir*. Reykjavík: Mál og Menning, pp. 49–58.

Guilbaud, M.-N., Self, S., Thordarson, T. & Blake, S. (2005). Morphology, surface structures and emplacement of lavas produced by Laki, AD 1783–1874. In: Manga, M. & Ventura, G. (eds) *Kinematics and Dynamics of Lava Flows. Geological Society of America, Special Papers* **396**, 81–102.

Hammer, J. E. & Rutherford, M. J. (2002). An experimental study of the kinetics of decompression-induced crystallization in silicic melt. *Journal of Geophysical Research* **107**, doi:10.1029/2001JB000281.

Hammer, J. E., Cashman, K. V. & Voight, B. (2000). Magmatic processes revealed by textural and compositional trends in Merapi dome lavas. *Journal of Volcanology and Geothermal Research* **100**, 165–192.

Harris, A. J. L., Flynn, L. P., Matias, O., Rose, W. I. & Cornejo, J. (2004). The evolution of an active silicic lava flow-field: an ETM+ perspective. *Journal of Volcanology and Geothermal Research* **135**, 157–168.

Harris, A. J. L., Bailey, J., Calvari, S. & Dehn, J. (2005). Heat loss measured at a lava channel and its implications for down-channel cooling and rheology. In: Manga, M. & Ventura, G. (eds) *Kinematics and Dynamics of Lava Flows. Geological Society of America, Special Papers* **396**, 125–146.

Helz, R. T., Heliker, C., Hon, K. & Mangan, M. T. (2003). Thermal efficiency of lava tubes in the Pu'u'O'o–Kupaianaha eruption. In: Heliker, C., Swanson, D. A. & Takahashi, T. J. (eds) *The Pu'u'O'o–Kupaianaha Eruption of Kilauea Volcano,*

Hawaii: the First 20 Years. US Geological Survey, Professional Papers **1676**, 105–120.

Herrmann, W. & Berry, R. F. (2002). MINSQ—a least squares spreadsheet method for calculating mineral proportions from whole rock major element analyses. *Geochemistry: Exploration, Environment, Analysis* **2**, 361–368.

Hon, K., Gansecki, C. A. & Kauahikaua, J. (2003). The transition from 'a'a to pahoehoe crust on flows emplaced during the Pu'u'O'o–Kupaianaha eruption. In: Heliker, C., Swanson, D. A. & Takahashi, T. J. (eds) *The Pu'u'O'o–Kupaianaha Eruption of Kilauea Volcano, Hawaii: the First 20 Years. US Geological Survey, Professional Papers* **1676**, 89–103.

Hoover, S. R., Cashman, K. V. & Manga, M. (2001). The yield strength of subliquidus basalts—experimental results. *Journal of Volcanology and Geothermal Research* **107**, 1–18.

Hui, H. & Zhang, Y. (2007). Toward a general viscosity equation for natural anhydrous and hydrous silicate melts. *Geochimica et Cosmochimica Acta* **71**, 403–416.

Hulme, G. (1974). The interpretation of lava flow morphology. *Geophysical Journal of the Royal Astronomical Society* **39**, 361–383.

Ishibashi, H. & Sato, H. (2007). Viscosity measurements of subliquidus magmas: alkali olivine basalt from the Higashi-Matsuura district, Southwest Japan. *Journal of Volcanology and Geothermal Research* **160**, 223–238, doi:10.1016/j.jvolgeores.2006.10.001.

Keszthelyi, L. & Denlinger, R. (1996). The initial cooling of pāhoehoe flow lobes. *Bulletin of Volcanology* **58**, 5–18.

Keszthelyi, L., Thordarson, T., McEwen, A., Haack, H., Guilbaud, M., Self, S. & Rossi, M. (2004). Icelandic analogs to Martian flood lavas. *Geochemistry, Geophysics, Geosystems* **5**(11), doi:10.1029/2004GC000758.

Keszthelyi, L., Self, S. & Thordarson, T. (2006). Flood lavas on Earth, Io and Mars. *Journal of the Geological Society, London* **163**, 253–264.

Kilburn, C. R. J. (1990). Surfaces of aa flow-fields on Mount Etna, Sicily; morphology, rheology, crystallization and scaling phenomena. In: Fink, J. H. (ed) *Lava flows and domes*, Berlin Heidelberg New York: Springer, pp. 129–156.

Kirkpatrick, R. J. (1981). Kinetics of crystallization of igneous rocks. In: Lasaga, A. C. & Kirkpatrick, R. J. (eds) *Kinetics of Geochemical Processes. Mineralogical Society of America, Reviews in Mineralogy* **8**, 321–395.

Kohut, E. & Nielsen, R. L. (2004). Melt inclusion formation mechanisms and compositional effects in high-An feldspar and high-Fo olivine in anhydrous mafic silicate liquids. *Contributions to Mineralogy and Petrology* **147**, 684–704.

Kouchi, A., Tsuchiyama, A. & Sunagawa, I. (1986). Effect of stirring on crystallization kinetics of basalt; texture and element partitioning. *Contributions to Mineralogy and Petrology* **93**, 429–438.

Lipman, P. W., Banks, N. G. & Rhodes, J. M. (1985). Degassing-induced crystallization of basaltic magma and effects on lava rheology. *Nature* **317**, 604–607.

Lofgren, G. (1974). An experimental study of plagioclase crystal morphology: isothermal crystallization. *American Journal of Science* **274**, 243–273.

Marsh, B. D. (1981). On the crystallinity, probability of occurrence, and rheology of lava and magma. *Contributions to Mineralogy and Petrology* **78**, 85–98.

Melnik, O. & Sparks, R. S. J. (2002). Dynamics of magma ascent and lava extrusion at Soufrière Hills Volcano, Montserrat. In: Druitt, T. H. & Kokelaar, B. P (eds) *The Eruption of Soufrière Hills Volcano, Montserrat, from 1995 to 1999. Geological Society, London, Memoirs* 21, 153–171.

Métrich, N., Sigurdsson, H., Meyer, P. S. & Devine, J. D. (1991). The 1783 Lakagigar eruption in Iceland; geochemistry, CO_2 and sulfur degassing. *Contributions to Mineralogy and Petrology* **107**, 435–447.

Métrich, N., Bertagnini, A., Landi, P. & Rosi, M. (2001). Crystallization driven by decompression and water loss at Stromboli Volcano (Aeolian Islands, Italy). *Journal of Petrology* **42**, 1471–1490.

Newman, S. & Lowenstern, J. B. (2002). VolatileCalc: a silicate melt–H_2O–CO_2 solution model written in Visual Basic for Excel. *Computers & Geosciences* **28**, 597–604.

Oze, C. & Winter, J. D. (2005). The occurrence, vesiculation, and solidification of dense blue glassy pahoehoe. *Journal of Volcanology and Geothermal Research* **142**, 285–301.

Peterson, D. W. & Tilling, R. I. (1980). Transition of basaltic lava from pahoehoe to aa, Kilauea Volcano, Hawaii: field observations and key factors. *Journal of Volcanology and Geothermal Research* **7**, 271–293.

Philpotts, A. R. & Carroll, M. (1996). Physical properties of partly melted tholeiitic basalt. *Geology* **24**, 1029–1032.

Pinkerton, H. & Stevenson, R. J. (1992). Methods of determining the rheological properties of magmas at sub-liquidus temperatures. *Journal of Volcanology and Geothermal Research* **53**, 47–66.

Polacci, M., Cashman, K. V. & Kauahikaua, J. P. (1999). Textural characterization of the pahoehoe–'a'a transition in Hawaiian basalt. *Bulletin of Volcanology* **60**, 595–609.

Polacci, M., Corsaro, R. A. & Andronico, D. (2006). Coupled textural and compositional characterization of basaltic scoria: insights into the transition from Strombolian to fire fountain activity at Mount Etna, Italy. *Geology* **34**, 201–204.

Putirka, K. D. (2005). Igneous thermometers and barometers based on plagioclase + liquid equilibria; tests of some existing models and new calibrations. *American Mineralogist* **90**, 336–346.

Ramsey, M. H., Potts, P. J., Webb, P. C., Watkins, P., Watson, J. S. & Coles, B. J. (1995). An objective assessment of analytical method precision: comparison of ICP-AES and XRF for the analysis of silicate rocks. *Chemical Geology* **124**, 1–19.

Saar, M. O., Manga, M., Cashman, K. V. & Fremouw, S. (2001). Numerical models of the onset of yield strength in crystal–melt suspensions. *Earth and Planetary Science Letters* **187**, 367–379.

Schiffman, P. & Lofgren, G. E. (1982). Dynamic crystallization studies on the Grande Ronde pillow basalts, Central Washington. *Journal of Petrology* **90**, 49–78.

Scholze, H. (1959). Der Einbau des Wassers in Glasern. *Glastechnische Berichte* **32**, 81–88, 142–145, 278–281.

Sigmarsson, O., Condomines, M., Gronvold, K. & Thordarson, T. (1991). Extreme magma homogeneity in the 1783–84 Lakagigar eruption; origin of a large volume of evolved basalt in Iceland. *Geophysical Research Letters* **18**, 2229–2232.

Sisson, T. W. & Grove, T. L. (1993). Experimental investigations of the role of H_2O in calc-alkaline differentiation and subduction zone magmatism. *Contributions to Mineralogy and Petrology* **113**, 143–166.

Soule, S. A. & Cashman, K. V. (2005). Shear rate dependence of the pahoehoe-to-'a'a transition; analog experiments. *Geology* **33**, 361–364.

Soule, S. A., Cashman, K. V. & Kauahikaua, J. P. (2004). Examining flow emplacement through the surface morphology of three rapidly emplaced, solidified lava flows, Kilauea Volcano, Hawai'i. *Bulletin of Volcanology* **66**, 1–14.

Sparks, R. S. J. (2003). Dynamics of magma degassing. In: Oppenheimer, C., Pyle, D. M. & Barclay, J. (eds) *Volcanic Degassing. Geological Society, London, Special Publications* **213**, 5–22.

Sparks, R. S. J. & Pinkerton, H. (1978). Effect of degassing on rheology of basaltic lava. *Nature* **276**, 385–386.

Sparks, R. S. J., Murphy, M. D., Lejeune, A. M., Watts, R. B., Barclay, J. & Young, S. R. (2000). Control on the emplacement of the andesite lava dome of the Soufrière Hills Volcano, Montserrat by degassing-induced crystallization. *Terra Nova* **12**, 14–20.

Stolper, E. (1982). Water in silicate glasses; an infrared spectroscopic study. *Contributions to Mineralogy and Petrology* **81**, 1–17.

Sugawara, T. (2000). Thermodynamic analysis of Fe and Mg partitioning between plagioclase and silicate liquid. *Contributions to Mineralogy and Petrology* **138**, 101–113.

Thordarson, T. & Self, S. (1993). The Laki (Skaftar Fires) and Grimsvotn eruptions in 1783–1785. *Bulletin of Volcanology* **55**, 233–263.

Thordarson, T., Self, S., Oskarsson, N. & Hulsebosch, T. (1996). Sulfur, chlorine, and fluorine degassing and atmospheric loading by the 1783–1784 AD Laki (Skaftar fires) eruption in Iceland. *Bulletin of Volcanology* **58**, 205–225.

Thordarson, T. L., Larsen, G., Steinthorsson, S. & Self, S. (2003). The 1783-1785 A.D. Laki-Grímsvötn eruptions II: Appraisal based on contemporary accounts. *Jökull* **53**, 11–48.

Thornber, C. R. (2001). Olivine–liquid relations of lava erupted by Kilauea Volcano from 1994 to 1998; implications for shallow magmatic processes associated with the ongoing east-rift-zone eruption. *Canadian Mineralogist* **39**, 239–266.

Tsuchiyama, A. (1985). Crystallization kinetics in the system $CaMgSi_2O_6$–$CaAl_2Si_2O_8$; development of zoning and kinetics effects on element partitioning. *American Mineralogist* **70**, 474–486.

Vance, J. A. (1969). On synneusis. *Contributions to Mineralogy and Petrology* **24**, 7–29.

APPENDIX

Table A1: Least-squares calculations of mineral proportions (vol.%)

Sample	Pl	Cpx	Ol	Glass	Cr.	$\sum R^2$	Sample	Pl	Cpx	Ol	Glass	Cr.	$\sum R^2$
15 08 83*	6·0	2·4	0·7	90·9	9·1	0·14	L63-10*	20·9	7·3	3·6	68·3	31·7	0·02
16 08 83*	6·4	1·8	1·1	90·7	9·3	0·16	L63-1*	20·5	6·3	3·8	69·4	30·6	0·07
18 08 83*	7·2	3·5	0·8	88·4	11·6	0·08	L63-5*	19·1	5·8	3·3	71·9	28·1	0·05
22 08 83*	6·3	2·4	0·7	90·6	9·4	0·08	L63-6*	21·8	7·3	3·5	67·4	32·6	0·20
L14-3*	15·3	3·8	3·0	77·9	22·1	0·06	L63-7*	19·9	6·2	3·2	70·6	29·4	0·08
L14-6*	16·8	4·2	3·4	75·6	24·4	0·04	L63-8*	19·8	6·6	3·3	70·4	29·6	0·07
L14-7*	14·4	4·0	2·9	78·7	21·3	0·05	L66-3*	19·1	6·9	3·0	71·0	29·0	0·04
L17-1*	17·5	4·9	3·3	74·3	25·7	0·03	L63-9 gl05	24·5	10·0	3·7	61·7	38·3	0·31
L17-3*	17·0	4·8	3·1	75·1	24·9	0·03	L63-9 gl01	24·7	10·8	3·5	61·0	39·0	0·40
L17-5*	15·9	4·7	2·6	76·8	23·2	0·03	L63-9 gl06	21·3	9·2	3·9	65·5	34·5	0·06
L17-6*	17·0	4·9	3·3	74·7	25·3	0·07	L63-9 gl31	23·3	11·1	3·2	62·4	37·6	0·30
E3-5*	22·9	7·9	3·9	65·3	34·7	0·04	L63-9 gl20	23·7	9·5	3·5	63·2	36·8	0·15
L4-2*	21·6	8·1	3·4	66·9	33·1	0·02	L63-9 gl21	23·0	10·8	4·1	62·0	38·0	0·14
L18-1*	21·5	7·2	3·6	67·7	32·3	0·10	L63-9 gl22	21·1	9·6	4·7	64·6	35·4	0·14
L21-1*	19·5	5·9	3·6	70·9	29·1	0·05	L63-9 gl23	26·4	11·2	3·9	58·5	41·5	0·36
L29-13*	21·1	7·4	3·4	68·1	31·9	0·07	L63-9 gl25	24·9	10·8	4·7	59·5	40·5	0·17
L29-15*	20·9	6·8	3·5	68·8	31·2	0·07	L63-9 gl26	27·3	12·6	4·6	55·6	44·4	0·29
L29-18*	20·4	7·2	3·4	69·0	31·0	0·04	L63-9 gl41	22·6	9·2	4·1	64·1	35·9	0·12
L33-1*	19·4	6·3	3·3	71·0	29·0	0·05	L63-9 gl42	26·4	10·2	3·8	59·5	40·5	0·44
L43-2*	19·3	5·5	3·3	71·9	28·1	0·09	L63-9 gl43	24·2	11·6	3·5	60·7	39·3	0·29
L55-10*	20·1	6·6	3·2	70·1	29·9	0·06	L63-9 gl44	23·1	8·9	4·0	64·1	35·9	0·10

*Average composition used.
Sample indicates glass composition used for calculations. Cr., total crystallinity. Results from calculations were converted from weight per cent to volume per cent using density of 2·6 for plagioclase (Pl), 3·3 for clinopyroxene (Cpx), 3·4 for olivine (Ol) and 2·75 for glass. Compositions used as parent composition and mineral components (including the glass considered) are reported in Table A2. A program by Herrmann & Berry (2002) iteratively adjusts proportions of mineral components to provide good fit with input parent composition. It returns sum of residuals squared ($\sum R^2$), which has to be <0·5 for the results to be acceptable.

Table A2: Parameters used in the least-squares calculations

Analysis no.	Sample type		SiO_2	TiO_2	Al_2O_3	FeO	MnO	MgO	CaO	Na_2O	K_2O	P_2O_5	Total
Sample composition													
WR2	whole rock		50·41	2·79	13·89	13·63	0·22	5·75	10·45	2·69	0·42	0·30	100·00
Minerals													
L7-5.12/6	ph plag	An^*_{76}	49·09	0·00	31·46	0·73	0·00	0·00	15·72	2·66	0·05		99·70
L63-7.66	gdm plag	An^*_{66}	52·74	0·00	29·48	0.91	0·00	0·20	13·30	3·79	0·10		100·50
L63-9.29	gdm plag	An^*_{55}	55·63	0·00	26·73	1·16	0·00	0·28	10·84	4·82	0·19		99·65
L7-5.3	ph ol	Fo_{71}	36·64	0·00	0·01	26·36	0·37	35·50	0·28	0·00	0·00		99·15
L63-9.33	gdm ol	Fo_{64}	37·00	0·11	0·05	30·86	0·46	31·34	0·45	0·01	0·00		100·28
L7-1.146	gdm cpx	En^*_{76}	50·55	1·13	3·28	8·65	0·21	15·20	20·35	0·29	0·00		99·64
L63-7.30	gdm cpx	En^*_{74}	51·37	1·20	3·28	9·42	0·24	15·07	19·57	0·32	0·01		100·47

Major elements reported in wt %. Sample type: ph, phenocryst; gdm, groundmass crystals, plag, plagioclase; ol, olivine, cpx, clinopyroxene. End-member mineral compositions were chosen avoiding primitive xenocryst-type compositions and crystals showing high amounts of minor elements. Small variations in the crystal compositions used had negligible impact on the results.